EXAFS on noble metal promoted Co/TiO_2

Internship Report

Masterprogramme: Nanomaterials: Chemistry & Physics

Utrecht University, The Netherlands

J. Oenema BSc

Supervisors:

Dr. G. Agostini (ESRF)

Dr. S. Pascarelli (ESRF)

Prof. Dr. F. M. F. de Groot (UU)

Dr. A. Pethoukov (UU)

Grenoble, June 2015

Contents

1. Introduction

During a 5 month project, noble metal promoted Co/TiO_2 catalysts for the Fischer-Tropsch process were studied with x-ray absorption fine structure techniques (XAFS). This project was performed during an internship at the ESRF in Grenoble from February to June 2015. The internship is part of the master program Nanomaterials: Chemistry & Physics at the University of Utrecht.

The catalyst that were studied are noble metal (Pt, Ag, Re, Ru) promoted Co/TiO_2 catalysts with a cobalt weight loading of approximately 9 wt. % and have a cobalt/noble metal ratio of 0.0143 at. The catalysts used during this project were synthesized and tested during a master project performed in the group of Inorganic Chemistry and Heterogeneous Catalysis before the internship. During this project, turnover frequencies were obtained by measuring the dispersion of the cobalt particles on the catalysts with transmission electron microscopy and catalytic tests under industrial conditions at a temperature of 220°C and a pressure of 20 bar. The noble metal promoted catalyst were found to have higher activities than the unpromoted catalysts. For the ruthenium, platinum and silver catalyst a threefold increase in the apparent turnover frequency was observed, while for the rhenium promoted catalyst a fourfold increase in the apparent turnover frequency was observed.[1,2] The aim of this project is to use XAFS to gain a deeper insight into the fundamental reasons of the increased activity of the noble metal promoted Co/TiO_2. By the average coordination number and the elements surrounding the noble metal atom, the location of the promoting noble metal was determined. From the EXAFS measurements on the platinum, ruthenium and rhenium promoted catalysts it was concluded that the noble metals were near or at the surface of cobalt particles. For the silver promoted catalyst, small silver particles of ~10 atoms appeared to be present on the surface of the catalyst.

2. Noble metal promoted Co/TiO_2 catalysts for the Fischer-Tropsch process

2.1 Introduction

The Fischer-Tropsch process describes the catalytic conversion of syngas (mixture of CO and H_2) into hydrocarbons. Syngas can be derived from a variety of feedstocks like: natural gas, coal and biomass. Generally, the synthesized hydrocarbons are further processed to ultra-clean fuels, lubricants or used as building blocks for polymers. The process was discovered in Germany by Franz Fischer and Hans Tropsch in 1923, and was intensively used during the Second World War as an alternative way of synthesizing fuel. In the 1960's the popularity of the process declined due to discovery of new oil fields and advances in oil drilling, which caused an increase in the worldwide availability of crude oil. However, starting from the 1980's the popularity of the process increased again, causing oil companies to invest in research and new Fischer-Tropsch plants. An example of a newly built Fischer-Tropsch plant is the Shell Pearl GTL plant in Las Raffan, Quatar (figure 1). The plant is estimated to break-even with gasoline derived from crude oil, at a crude oil price of $ 36 per barrel.[3–5]

Figure 1: Shell Pearl Gas to Liquids (GTL) plant in Las Raffan, Quatar. In is the largest GTL plant in the world with a maximum production of 140.000 barrels of liquid products per day.[6]

2.2 Drivers for use of the Fischer-Tropsch process

The renewed interest in the process since the 1980's is caused by a number drivers:

- The increasing worldwide demand for (liquid) fuels, caused by an increased worldwide energy demand. The availability of liquid fuels is highly dependent on the availability of crude oil which has shown to be very volatile in the last decades, causing a fluctuating oil price.[7] The Fischer-Tropsch process can be seen as an alternative route to obtain liquid fuels, independent on the availability of crude oil.
- The depletion of the worldwide crude oil reserves causes oil companies to think of other feedstocks for liquid fuels. The currently know reserves of crude oil, assuming a constant demand, are sufficient for approximately 50 years.[7]
- A number of gas fields are considered as stranded because it is not economically viable to recover the gas, which implies the construction of a costly pipeline infrastructure. The Fischer-Tropsch process can be used to recover the natural gas from these gas fields and convert it into fuel which can be shipped.[8]
- The possibility to synthesize ultra-clean automotive fuels which are necessary to increasingly stringent environmental legislation. Fuel derived from crude oil often contains contaminations like: sulfur species, aromatics and hetero-atom aromatics. Ultra-clean fuel from the Fischer-

Tropsch process can be mixed with fuel derived from crude oil to reduce the emission sulfur oxides, and by more efficient combustion properties also the emissions of particulate matter and carbon monoxide can be reduced.[9,10]
- The possibility to synthesize large hydrocarbons which can be used directly as specialty chemicals or are further converted into products such as lubricants. Specialty chemicals have a higher profit margin than fuel and can therefore be used to increase the profitability of a Fischer-Tropsch plant.

2.3. The Fischer-Tropsch reaction and catalyst composition

During Fischer-Tropsch synthesis hydrocarbons of different length and structure are formed by surface polymerization on metallic nanoparticles. The catalytic metals usually used for Fischer-Tropsch synthesis are iron or cobalt. The catalysts that are studied during this project are titania supported cobalt nanoparticles, which have a high selectivity towards long hydrocarbon chains. Another advantage of cobalt over iron is that it has a low activity in the water-gas shift reaction.

The prevailing reactions during synthesis are:

n-alkanes: $\mathrm{n\,CO} + (2\mathrm{n}+1)\,\mathrm{H_2} \rightleftarrows \mathrm{C_nH_{(2n+2)}} + \mathrm{n\,H_2O}$ $\Delta H° = -165\ \mathrm{kJ{\cdot}mol^{-1}}$

α-alkenes: $\mathrm{n\,CO} + 2\mathrm{n\,H_2} \rightleftarrows \mathrm{C_nH_{(2n)}} + \mathrm{n\,H_2O}$ $\Delta H° = -165\ \mathrm{kJ{\cdot}mol^{-1}}$

These reactions are highly exothermic: the formation of one mole of the building block CH_2 generates 165 kJ of heat. The range of C_5-C_{16} hydrocarbons is in the form of liquids, while C_{16+} hydrocarbons are in the form of wax at room temperature. The main side products are methane and short α-alkenes which are usually in the C_2-C_6 range. Cobalt catalyzed Fischer-Tropsch synthesis is performed industrially between 200-250°C and at 20 bar.[4,10]

A typical industrial catalyst for cobalt based Fischer-Tropsch consists of at least four different components:

- Cobalt as the **active metal** (8-30 wt.%)
- **Support** which is usually a refractory metal oxide
- **Reduction promoter** which is usually a noble metal (0.05-1 wt.%)
- **Structural promoter** which is usually a metal oxide (1-10 wt.%)

During this project the effect of noble metal promotion on titania supported cobalt nanoparticles is studied. Noble metal promoters have multiple effects on the performance of cobalt based Fischer-Tropsch catalyst, which can be divided in structural, electronic or synergistic effects. Structural promoters affect the formation and stability of the active phase of a catalyst, whereas electronic promoters directly affect the elementary steps involved in each turnover on the catalyst. A synergistic promoter improves catalyst performance by inhibiting the deactivation of the catalyst during synthesis.[11,12]

2.4 Structural and Synergistic effects of noble metal promotion

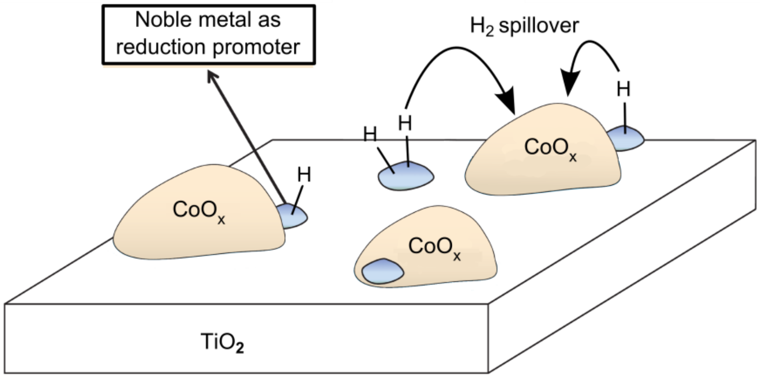

Figure 2: Hydrogen spillover on the surface of a noble metal promoted Co/TiO_2 Fischer-Tropsch catalyst. The image was reproduced from [4]. (Image was modified afterwards).

The most eminent structural effect of the addition of noble metal promoters is the decrease of the cobalt oxide reduction temperature. During a catalyst activation procedure using a reducing gas, noble metal oxides are reduced at low temperatures (100-200°C), while cobalt oxides reduce at (250-350°C).[13] However, a noble metal present on the catalyst support can facilitate the reduction of cobalt oxide by hydrogen spillover (figure 2). When a H_2 molecule adsorbs on a noble metal particle, it forms mononuclear hydrogen which can migrate over the surface to cobalt oxide particles and thereby reducing cobalt oxide. The reduction of cobalt oxide at lower temperatures is therefore facilitated by the presence of noble metal species. A lower reduction temperature of a catalyst can reduce the energy costs of activation which can be of great importance when Fischer-Tropsch catalysts are applied on a large scale.[11,14] Enhancement in cobalt dispersion is another structural effect due to introduction of noble metals to cobalt catalysts. A better dispersion of cobalt particles was reported for catalysts promoted with rhenium, ruthenium, palladium and platinum.[5,11]

Noble metal promotion of cobalt Fischer-Tropsch catalyst on a reducible support can lead to an increase in the activity of the catalyst, caused by a synergistic effect between cobalt and the noble metal. Iglesia et al. reported such an bimetallic synergy in 1993 for 11.3 wt.% cobalt supported on titania promoted with 0.14 wt.% Ru (figure 3).[12] The article reports a threefold increased turn over frequency of $1.7 \cdot 10^{-3}\ s^{-1}$ for the unpromoted catalyst, to $5.3 \cdot 10^{-3}\ s^{-1}$ for the ruthenium promoted catalyst (Co/Ru = 0.0063 at.). According to the authors, the improved activity and selectivity arise from a Ru-promoted cleansing of cobalt surface ensembles during Fischer-Tropsch synthesis. Ruthenium catalyzes the hydrogenolysis of carbonaceous residues and reduces of surface oxygen species which permits regeneration of these bimetallic catalysts using H_2.

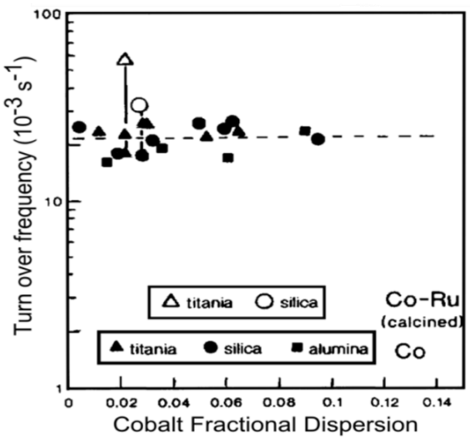

Figure 3: The turn over frequency plotted versus the cobalt fractional dispersion. The unpromoted catalyst have a turn over frequency of ±$2.0\cdot10^{-3}$ s^{-1}, while the Co/TiO_2 promoted with Ru has a threefold higher turnover frequency of: $5.3\cdot10^{3}$ s^{-1}. Reproduced from:[12].

Also on rhenium promoted cobalt catalyst supported on titania an threefold increased turn over frequency was reported by Storsæter et al.[15] The explanation of the authors was that rhenium promotion lead to an increased reducibility and increased number of surface exposed cobalt atoms. The results of Iglesia and Storsæter were confirmed in the preceding master project (figure 4). For the catalysts promoted with platinum, silver and ruthenium and with a cobalt/noble metal ratio of 0.0143 at., a threefold increase in apparent turnover frequency was observed. For the rhenium promoted catalyst with the same cobalt/noble metal ratio a fourfold increase in turnover frequency was observed.[1,2]

Besides the results on titania, there are many catalytic test results in literature of noble metal promoted cobalt Fischer-Tropsch catalyst supported on alumina and silica, which have an increased activity in Fischer-Tropsch synthesis. This is usually ascribed to an increased degree of reduction and higher cobalt dispersion leading to an increased number of surface exposed cobalt atoms.

In order for a noble metal to work as a reduction promoter via H_2 spillover or a synergistic promoter, it is essential that noble metal atoms are present at or near the surface of cobalt particles. In determining the location and chemical environment of the noble metals on the catalyst EXAFS proves to be a very useful technique. Many articles in literature report XANES/EXAFS studies on noble metal promoted cobalt Fischer-Tropsch catalysts, of which a short summary is given below.[14]

Two articles by Davis et al. and Holmen describe EXAFS measurements on rhenium promoted Co/Al_2O_3.[16,17] In both cases the catalysts were synthesized by incipient wetness impregnation, and dried and calcined/heat-treated afterwards. Both studies report the presence of Co-Re chemical bonds while no direct Re-Re bonding contribution was observed. This leads to the conclusion that rhenium is located within cobalt particles or present at the surface, isolated from other Re atoms. Holmen reported that the intimate contact with the cobalt oxides may facilitate the reduction of cobalt oxides at lower temperatures by H_2-spillover.

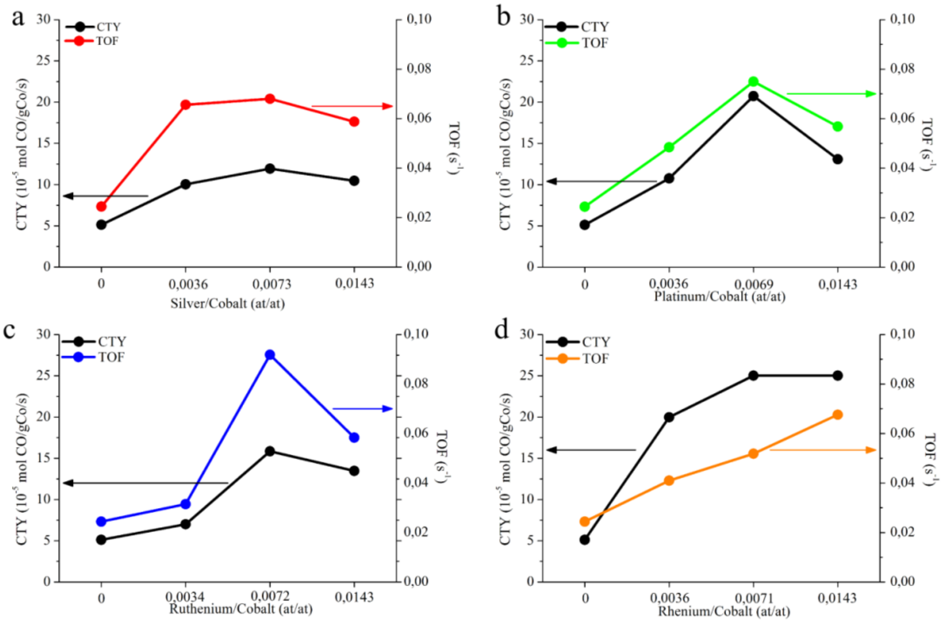

Figure 4: Catalytic test results from the different catalysts promoted with: silver (a), platinum (b), ruthenium (c), rhenium (d). The cobalt time yield, the activity per gram of cobalt is indicated in black. The colored lines indicate the TOF, the activity normalized for the amount of active sites. Note that during this project only the catalysts with the highest promoter loading were tested during this project.

Iglesia et al. have reported EXAFS measurements on ruthenium promoted Co/TiO_2 during a calcination procedure. The catalyst was prepared via sequential impregnation with cobalt and ruthenium precursor solutions. After the drying procedure to evaporate the solvent of the precursor solution, only Ru-O and Ru-Ru interactions were observed in the EXAFS spectrum. When EXAFS measurements were made during the calcination treatment, Co-Ru interactions became apparent with increasing coordination number at increasing calcination temperatures. The authors concluded that the ruthenium is incorporated in the cobalt particles during reduction and is located near outer crystallite surfaces.

Davis et al., reported the presence of Co-Pt interactions in platinum promoted Co/Al_2O_3. The authors concluded that the platinum atoms must be in intimate contact with the cobalt cluster to account for the observed Fourier transform of the coordination shells. Besides that, there was no sign of Pt-Pt interactions in the EXAFS pattern of the catalyst in reduced state.[18] The presence of Co-Pt interactions on platinum promoted Co/SiO_2 was also confirmed by a XRD study by Dees et al.[19] Therefore, the formation of Co-Pt bonds seems to be occurring for all platinum promoted cobalt catalysts, regardless of the support and the metal support interactions.

Davis et al. made a comparison between platinum and silver promoted Co/Al_2O_3, to study the use of silver as a substituent for platinum on an industrial scale. Besides of forming a cobalt-noble metal alloy, the authors report Ag-Ag coordination on the silver promoted Co/Al_2O_3. Moreover the fraction of Ag in coordination with Co decreases as a function of Ag promoter loading, revealing that the interaction of Ag with Co is not as high as in the case other noble metals such as: Pt, Ru and Re. The tendency of silver to form a separate phase on silver promoted cobalt catalysts was confirmed by Jacobs et al.[20] Jacobs also studied fellow group 11 metals: copper and gold as promoters for Co/Al_2O_3 whichs also formed separate phases.

So far, no EXAFS/XANES results have been reported on platinum and silver promoted titania supported cobalt Fischer-Tropsch catalysts.

3. Theory of XAFS

3.1 Introduction to XAFS

X-ray Absorption Fine Structure spectroscopy (XAFS) is a technique that provides information on the electronic and structural properties of samples by using x-rays. The technique allows to study the details of how x-rays are absorbed by atoms at energies near and above the core-level binding energies of electrons. If the energy of the x-ray photon is equal or higher than the binding energy of the electron, the x-ray is absorbed by the so-called photoelectric effect. The sudden increase in absorption when going from a photon energy below the binding energy to an energy higher than the binding energy, is visible as a jump in the absorption spectrum. The information that can be obtained from an XAFS spectrum is: the formal oxidation state, the coordination chemistry, the coordination number and species of the atoms immediately surrounding the absorber atom.[21,22]

To insure a high resolution of the absorption spectra, an intense and energy-tunable source of x-rays is required, which is often provided by a synchrotron. The intrinsic properties of the synchrotron and the properties of the experimental station dictate what energy ranges, beam sizes and intensities are available. This puts practical experimental limits on the measurements such as e.g.: what elements and what energy levels can be measured. Light elements such as carbon and oxygen have low binding energies of electrons in the K-shell, whereas heavy elements such as platinum and gold have higher binding energies for the K-shell and lower binding energies for the L-shell. Sometimes, in the case of very heavy elements, the electrons from the M-shell are used as probe.[21–23]

Compared to other x-ray techniques, XAFS measurements are relatively straightforward, because it is an atomic probe. Therefore, it places few constraints on the samples that can be studied. XAFS measurements of catalysts can be performed in-situ under reaction conditions and in the presence of reactants. Many experimental techniques and sample conditions are available for XAFS such as: very fast measurements of in-situ chemical processes, high spatial resolution and extreme conditions of temperature and pressure.[23,24] Because synchrotron x-rays have a high intensity, the beam penetrates through the sample, making XAFS a ‘bulk’ technique without surface selectivity. In some cases, special measurement techniques can be applied to enhance the surface selectivity. For instance, an element which is only present at the surface can be studied.[21,23]

3.2 The photo electric effect

3.2.1. Absorption

X-rays are a form of electromagnetic radiation of a wavelength between 0.0025 - 250 nm or an energy between 5 eV and 500 keV. In this range of energy, light or electromagnetic radiation can be absorbed by all matter by the photoelectric effect. The absorption of x-rays can be described by an exponential law in which I is the intensity of x-rays, x is the sample thickness and μ is the absorption coefficient (equation 1).

$$I = I_0 e^{-\mu x} \qquad (1)$$

For x-rays, as for all light, the x-ray intensity is proportional to the number of x-ray photons. The absorption coefficient μ is depends on the energy of the x-rays and the composition and density of the sample (equation 2).

$$\mu \approx \frac{\rho Z^4}{AE^3} \qquad (2)$$

In this formula shows the dependences of the absorption coefficient μ, in which: ρ is the density of the sample, Z is the atomic number, A is the atomic mass and E is the energy of the x-rays.

As can be seen from the formula, the absorption is highly dependent (E^3) on the x-ray energy. When the energy of the absorbed x-ray photons increases, the absorption coefficient μ(E) progressively decreases. This can be explained by the fact that harder, more energetic, x-rays are more penetrating than softer x-rays. Furthermore, the absorption is also highly dependent on the atomic number (Z^4). This can be explained by the fact that heavier, larger atoms are more absorbing, because they have more electrons which can be excited.

The absorption coefficient as function of the photon energy of any given element is a smooth curve, which is interrupted by absorption edges. These edges are caused by the photo electric absorption of x-rays by electrons from tightly bonded core levels. The x-ray absorption edges are defined by the alphabetical letters: K, L and M corresponding to the principal quantum numbers: n = 1, 2 and 3, respectively. The K edge (n = 1, ℓ = 0) corresponds to the 1s orbital and is the first electron level and has the highest binding energy. The next consecutive edges, corresponding to quantum numbers n = 2 and ℓ = 0 or 1, are the three L edges. The L_I, L_{II} and L_{III} edges correspond to the extraction of an electron from the 2s, $2p_{1/2}$ or $2p_{3/2}$ orbitals, respectively. The difference between the L_{II} and the L_{III} edge, which share the n and ℓ quantum number, is due to the large effect of the spin orbit splitting. For the $2p_{1/2}$ the spin and the angular momentum are aligned in opposite directions while for the $2p_{3/2}$ the spin and the angular momentum are aligned in the same direction. The M shell is sometimes probed for very heavy elements, for which the K and L edges are too high in energy to be excited by x-rays. The M shell corresponds to quantum numbers n = 3 and ℓ = 0, 1 or 2 which correspond to the 3s, 3p and 3d orbitals.

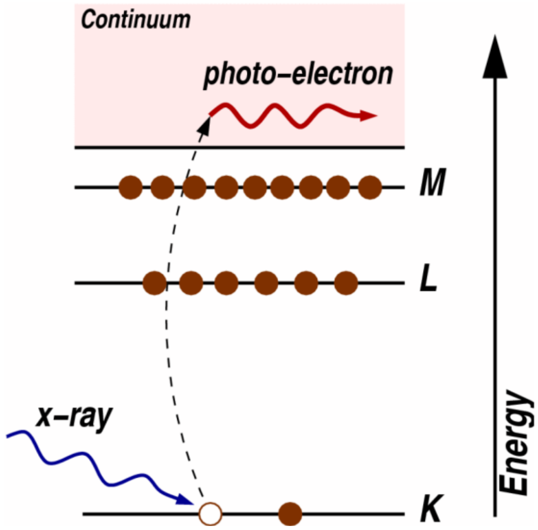

Figure 5: Schematic representation of the electronic structure while an electron is excited. Reproduced from: [21].

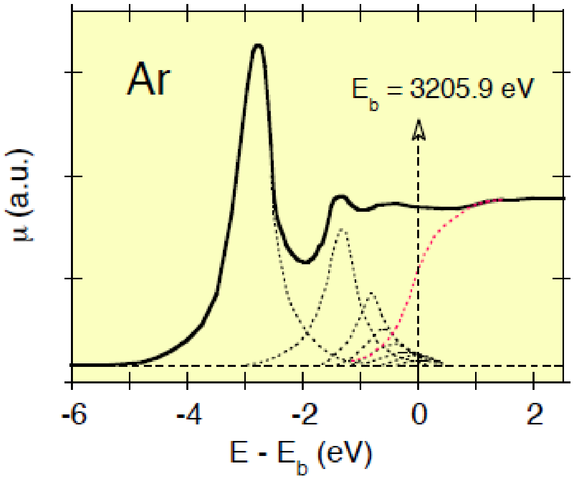

Figure 6: Absorption spectrum of Argon. Reproduced from: [25].

Upon absorption of an x-ray photon, the core electron is either, depending on the x-ray photon energy, excited to an upper unoccupied bound level or ejected out of the atom into the continuum (ionization). In figure 5 the ejection of an electron to the continuum can be seen while in figure 6 the absorption spectrum of the K edge of argon can be seen. The absorption signal has been ‘deconvoluted’ to show the contributions of the individual electron transitions. The black dotted lines show the contributions of the filling of the upper unoccupied levels while the red line shows the contribution of the ejection of the electron. The upper levels are occupied when the energy of the x-rays is a few eV below the binding energy and are called the Rydberg levels. The occupation of the first Rydberg level leads to the first absorption peak. The minimum energy necessary to eject the electron from the atom is equal to the binding energy of the core electron. In figure 6 the binding energy of the core electrons has been referred to as E_b. When the atom is ionized, the atom is in an excited state with an empty electronic level near the core (core hole). The excess of energy of the x-ray above the binding energy E_b, is given to the photoelectron in the form of kinetic energy E_k. The kinetic energy of the electro-photon can be calculated with the formula 3.

$$E_k = E - E_b = \frac{p^2}{2m} = \frac{\hbar^2 k^2}{2m} \qquad \lambda = \frac{2\pi}{k} \qquad (3)$$

3.2.2. De-excitation

The excited atom will eventually relax to a stable ground state. This de-excitation can occur via two mechanisms: Fluorescence or Auger emission. In the fluorescence mechanism an electron from a higher energy level decays, emitting a fluorescent photon with an energy determined by the difference between the higher lever and the core-level. Radiation generated by decaying electrons coming from the L level is called K_α radiation, while the radiation generated by electrons from the M level is called K_β radiation, as can be seen in figure 7. In the Auger mechanism an electron from a higher level decays, filling the core level and in the meantime an electron from a higher level is ejected from the atom. This excited electron has a potential energy determined by the difference of decay of the electron that fills the core hole. Auger emission dominates below a x-ray energies below 2 keV, whereas at higher energies fluorescence is more likely to occur. Both the fluorescent x-rays and the electrons from the Auger emission can be detected, and by applying a fixed geometry the absorption coefficient can be determined.

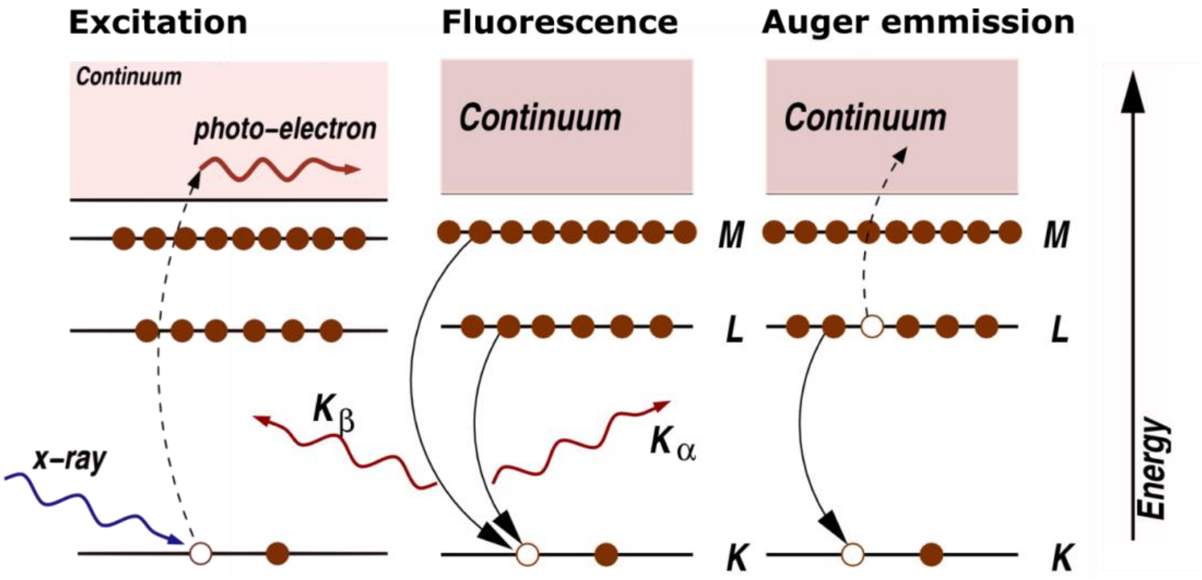

Figure 7: Schematic representation of excitation, fluorescence and Auger emission. Reproduced from:[21]**.**

3.3 The XAFS spectrum

A x-ray absorption fine structure spectrum consists of two regions: a XANES and an EXAFS region. (figure 8) The structure within 30-50 eV above the edge is called the X-ray Absorption Near Edge Structure (XANES). Sometimes, this structure is also referred to as edge structure or white line. From this region information can be obtained about the local atomic structure as well a geometric structure. The term white line originates from a few decades ago, when x-ray sensitive films were used to determine the absorption coefficient. The XANES is caused by core electron transitions to unfilled bound states, nearly bound states and to a low extent, transitions to the continuum. Presence of neighboring atoms next to the absorber atoms can lead to X-ray absorption Fine Structure (XAFS). The fine structure is visible in the absorption spectrum as an oscillatory variation of the X-ray absorption as a function of photon energy, beyond an absorption edge. The fine structure extending from the XANES region up to typically one thousand eV from the edge is called the Extended x-ray Absorption Fine Structure (EXAFS). The EXAFS carries information on the local geometric structure surrounding a given atomic species. For isolated atoms (noble gases, metallic vapors) EXAFS oscillations are limited to a few eV around the edge, and reflects the transitions of the core electron to higher unoccupied levels. In molecular gases and condensed systems the EXAFS, strongly influenced by the presence of the atoms surrounding the absorber, can extend up to one thousand eV above the edge.

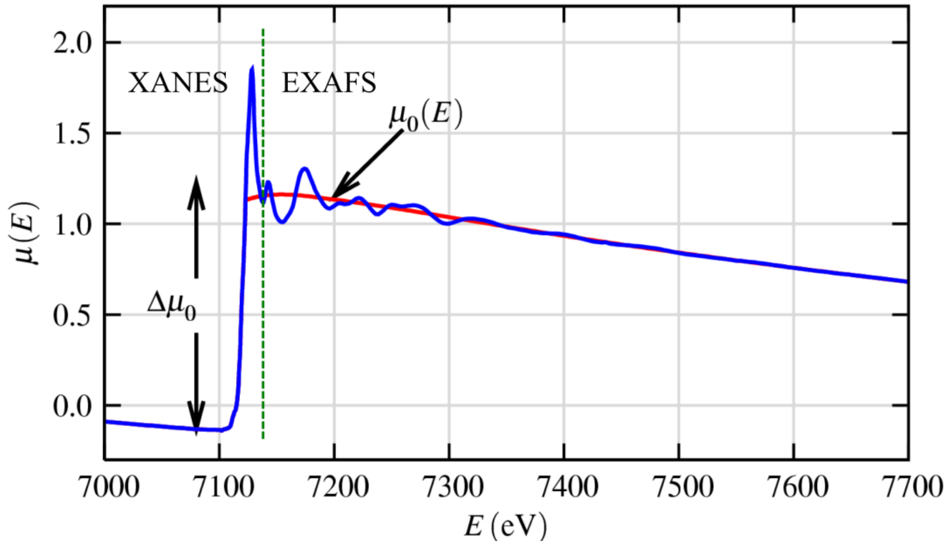

Figure 8: An example of an XAFS spectrum of FeO. Reproduced from:[21]**.**

3.4 The fundamental principles of EXAFS

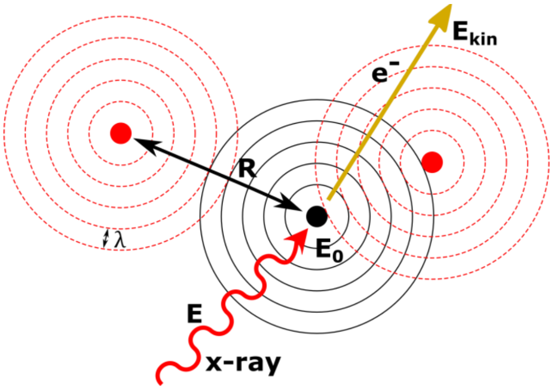

Figure 9: An incoming x-ray exciting a core level electron.

EXAFS oscillations are caused by neighbouring atoms coordinated around the absorber atom, for instance in molecular gasses and condensed matter. Neighboring atoms around the absorber atom can cause the ejected photo-electron to be back-scattered. This can lead to an incoming spherical wave which interferes with the outgoing spherical wave (figure 9). The interference leads to fine structure oscillations in the absorption coefficient after the edge. The absorption coefficient μ depends on the so-called dipole matrix element between an initial core state ψ_i and the photo-electron state ψ_f. The dipole matrix element is a superposition (summation) of the incoming and the outgoing waves. These oscillations are described by formula 4.

$$\mu_0(\omega) \propto \left|\langle\psi_i|\hat{\eta}\cdot\boldsymbol{r}|\psi_f^0\rangle\right|^2 \qquad (4)$$

In the formula r is the vector position and $\hat{\eta}$ the polarization unit vector. The frequency of EXAFS oscillations depends on the distance between absorber and back-scatterer atoms. From the distance between the atoms a distinction can be made between the different types of neighboring atoms. The amplitude of the oscillations is proportional to the number of back-scatterer atoms. The phase relationship between outgoing and incoming waves depends on photo-electron wavelength and inter-atomic distance R (figure 10). The variation of phase relationship as a function of photon energy influences the final state amplitude at the core site, giving rise to an interference phenomenon which modulates the absorption coefficient. The distances between the absorber atoms and the neighboring atoms, strongly modulates the absorption coefficient. The probability of absorption oscillates due to constructive and destructive interference.[25]

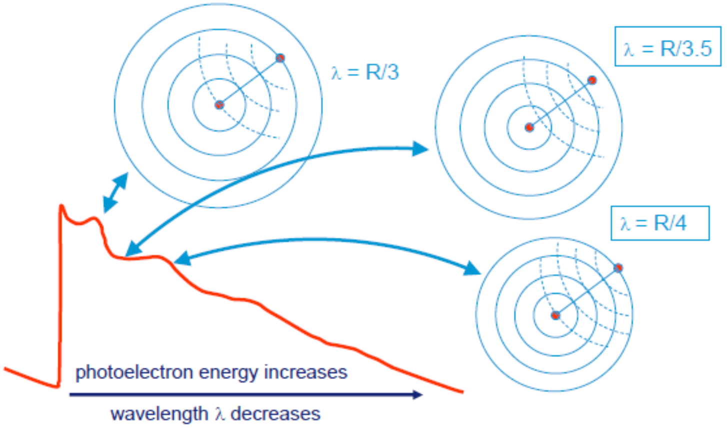

Figure 10: Different oscillations in the absorption spectrum can be seen. Reproduced from: [26]

3.5 XAFS measurements

During a XAFS measurement the sample is placed directly in the x-ray beam (figure 11), and the absorption is determined by either measuring the transmitted signal or the fluorescence yield.

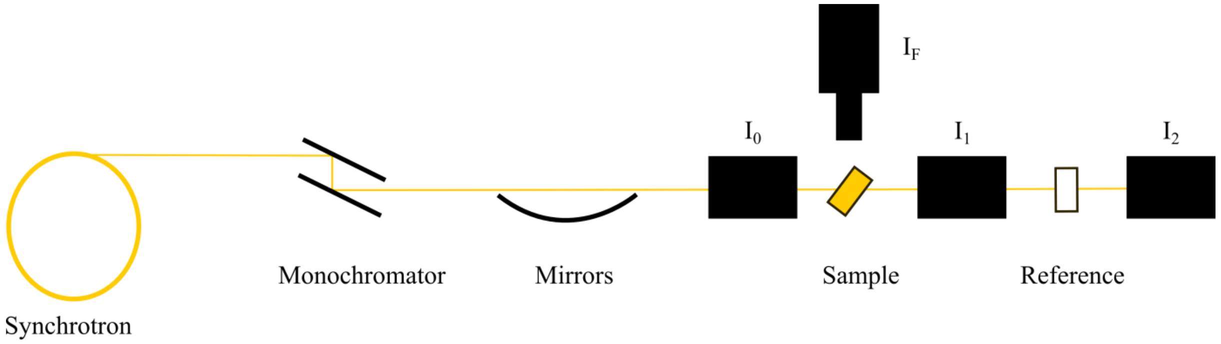

Figure 11: Schematic representation of the experimental set-up of BM23 at the ESRF.

3.5.1. Transmission measurements

When a beam of x-ray photons passes through the sample, photons will be absorbed by the sample leading to a lower intensity (I) of the transmitted x-ray beam. The transmission signal is usually obtained by using two ionization chambers, before (I_0) and behind (I_1) the sample. The I_1 is the signal coming from the sample, while the I_0 is used as reference. By using Lambert-Beer's law, the absorption coefficient μ(E) can be calculated (Eq. 5).

$$\mu(E) = -x ln\frac{I_1}{I_0} \qquad (5)$$

In equation 5, x is the sample thickness in cm. The intensities I_1 and I_0 have a value between 0 and 1 and are unitless. The absorption coefficient $\mu(E)$ is expressed in cm^{-1}.

During a transmission measurement it is a common practice to measure a reference foil of the probed element simultaneously. The reference foil is placed behind the I_1 ionization chamber as can be seen in figure 11. In this case the signals from I_1 and I_2 are used to calculate the absorption coefficient μ(E). The advantage of this kind of referencing is to be able to correct for any distortions during the experiment which are not caused by the sample.

The ionization chambers consist of a gas filled chamber with two electrodes: an anode and a cathode, with a voltage applied between them. The gas is ionized upon absorption of an x-ray photon and the subsequent ions are drawn towards the electrodes of opposite polarity, causing a small ionization current. This current can be detected by a (sensitive) electrometer circuit. The sensitivity of the ion chambers is determined by the gas pressure and the type of gas in the ionization chamber. Usually inert and/or noble gasses are used because they ensure stable measurements. Gasses with a higher molecular weight are used for measurements at higher x-ray energies, because gasses with a higher molecular weight are able to absorb (more) photons of higher energies.

The advantages of a transmission measurements are that the 'true' x-ray signal of the sample is used, which means that there are few distortions in the signal and high k-ranges are possible. The disadvantages are that it is not sensitive for very diluted systems, because the absorption is not detectable in relation to the intensity of the x-ray beam. Other disadvantages are that the sample should be homogeneous, free of pinholes and have a correct thickness in order to perform successful measurements.[21]

3.5.2. Fluorescence measurement

When a transmission measurement is not possible because the sample is very diluted or doesn't have the correct thickness, a fluorescence measurement can be performed. A fluorescence measurement differs fundamentally from a transmission measurement, because the x-ray absorption is determined indirectly by probing the fluorescent de-excitation. When the core hole is refilled with an electron from a higher shell, a fluorescent photon is emitted whit an energy equal to the difference in binding energy between the two shells. These fluorescent photons can be detected with a fluorescent detector which usually works with a CCD chip. The x-rays emitted from the sample will include the fluorescence line of interest, fluorescence lines from other elements in the sample, and both elastically and inelastically scattered x-rays. The fluorescence is emitted isotropically (in all directions) while the scatter is not emitted isotropically because the x-rays from a synchrotron are polarized in the plane of the synchrotron. The polarization means that elastic scatter is greatly suppressed at an angle of 90° from the beam. Therefore fluorescent detectors are normally placed at a right angle to the incident beam (figure 11). Because the detector detects only a fraction of the fluorescent photons (I_F) and not the 'true' fluorescent signal, the logarithm of the Lambert-Beer law cannot be used. Therefore, a fluorescence geometry is used to determine the absorption coefficient (equation 6). The I_0 is determined by the ionization chamber before the sample.[21]

$$\mu(E) \sim \frac{I_F}{I_0} \qquad (6)$$

3.6 A synchrotron x-ray source

A synchrotron is a source of x-rays of high energy and brilliance which is ~10^{14} times more powerful than convential x-ray sources, such a x-ray tubes. In order to generate x-ray's, electrons are injected into the booster synchrotron by the linear accelerator (Linac, see figure 12). In the booster synchrotron the electrons are accelerated up to operating energy of the storage ring and thereafter periodically injected into the storage ring. The storage ring consists of a circular vacuum tube with insertion devices or bending magnets and alternately, focusing magnets or undulators. The bending magnets and insertion devices are able to bend the direction of the electrons in the ring and, as a consequence, the electrons emit x-rays. These highly brilliant and polychromatic x-rays are directed towards the beamline behind each bending magnet or insertion device. By the emission of x-rays the electron loses energy, which is recovered by the undulators, also called RF cavities, enabling the electron beam to maintain it's working energy. Furthermore, focusing magnets are used to focus the beam of the storage ring, to minimize intensity losses.[22,27]

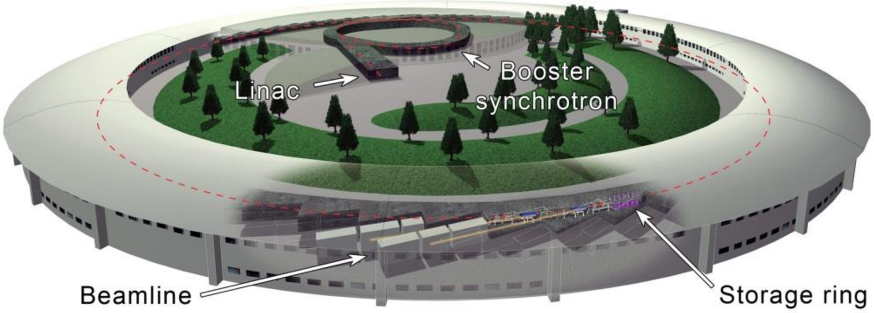

Figure 12: The ESRF synchrotron consist of a Linac, Booster synchrotron and the Storage ring. Reproduced from:[27].

The x-rays are generated by an insertion device or an bending magnet which work in different ways.

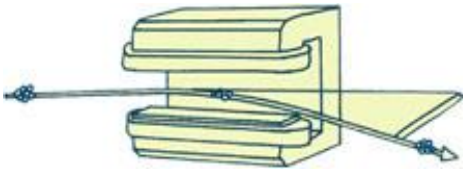

Figure 13: An electron beam going through a bending magnet. Reproduced from:[27].

A bending magnet consists of two magnets on opposite sides of the electron beam (figure 13). The magnet deflects the electrons from their straight trajectory, during which the electrons emit x-rays in different angles between the new trajectory and the normal of the original trajectory. The light from a bending magnet covers a wide and continuous spectrum of x-rays. After the bending magnet, the x-rays are led through a beamline in which the x-ray beam is focused.[27]

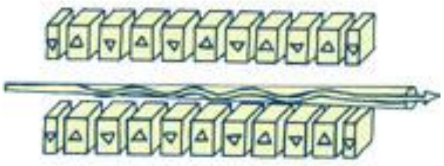

Figure 14: An electron beam going through an insertion device. Reproduced from:[27].

An insertion device consists of two arrays of small magnets of alternating polarity, which forces the electrons to follow an undulating trajectory (figure 14). The radiation emitted at each consecutive bend overlaps and interferes with that from other bends, forming a x-ray beam with photons which are concentrated at certain energies, corresponding to the individual magnets of the insertion device. The gap between the rows of magnets can be changed to fine-tune the wavelength of the x-rays in the beam. Compared to a bending magnet, an insertion device produces more brilliant and more focused x-ray beam.[27]

After each bending magnet or insertion device a mono- or polychromator is placed to select the x-ray wavelength. A monochromator is usually made from one or more pairs of silicon plates with different lattice spacing (111,311,511). By changing the angle of the silicon plates with respect to the beam using Bragg diffraction a particular x-ray energy can be selected (equation 8). The principle characteristics of a monochromator that are important for XAFS are the energy resolution, the reproducibility and stability of the monochromator. Energy resolutions of 1 eV at 10 keV are readily achieved with silicon monochromators, and sufficient for XAFS. Stability and reproducibility of the monochromator is sometimes more challenging to control. For the most part, these features are generally set by the beam-line, and are generally quite good at beam-lines designed for XAFS measurements.

$$n\lambda = 2dsin(\theta) \qquad (7)$$

4. Theory of data analysis of XAFS

Before a x-ray absorption spectrum can be analyzed, the absorption μ(E) needs to be calculated from the measured intensities. The calculation is usually performed by the software of the beamline by using Lambert-Beer's law. The absorption signal of the sample is transferred to a data file, which can be used by a beamline user for further analysis. There are many different methods and software packages available for analyzing the absorption signal.

To convert the measured signals into usable data, the data needs to be converted. This is usually done by the following steps[21,28]:

1. The measured intensities are converted into μ(E) by Lambert-Beer's law and plotted versus the x-ray energy (eV).
2. The pre-edge of the absorption spectrum is corrected by subtraction of a smooth pre-edge function, to get rid of experimental background and absorption from other edges. An example of a smooth pre-edge line can be seen in figure 15.

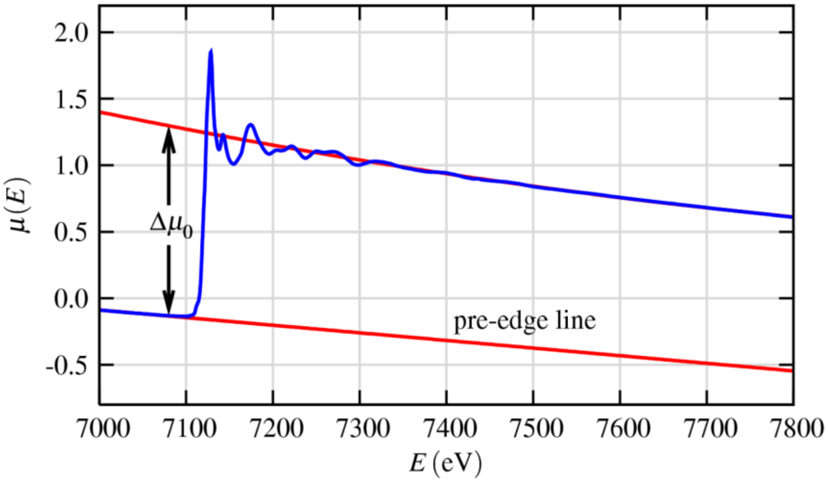

Figure 15: An x-ray absorption spectrum with the pre-edge line and the absorption jump indicated as $\Delta\mu_0$.

3. The μ(E) is normalized to go from 0 to 1 by using the approximated absorption jump $\Delta\mu_0$. By normalizing the spectrum in this way, it corresponds to the absorption of 1 x-ray.
4. The post-edge region is corrected by subtraction of a smooth post-edge background function corresponding to the absorption of an isolated atom, called $\mu_0(E)$.
   Steps 3 and 4 are can be summarized in the so-called EXAFS equation.

$$\chi(k) = \frac{(\mu-\mu_0)}{\Delta\mu_0} \qquad (8)$$

5. The edge position E_0 is determined: a common definition of the E_0 is the maximum of the derivative of the μ(E). Thereafter, convert the signal from E to k space by using formula 10. Furthermore the k weight is determined to amplify oscillations at high k values. Usually for heavier atoms like Pt and Re a k weight of 3 (k^3) is used.

$$k = \frac{\sqrt{2m(E-E_0)}}{\hbar^2} \qquad (9)$$

6. The range of useful signal of the $\chi(k)$ is determined and with this signal a Fourier transform is performed from k to real (R) space.
7. Isolate the $\chi(k)$ for an individual “shell” by backwards Fourier filtering. The oscillation of a single shell is plotted in k space (sometimes called q space).

These step result in different plots of an EXAFS scan, containing qualitative information about the atoms surrounding the absorber atom. In order to obtain quantitative information, a fit must be made of the spectra with a computed model of the studied system. The information that can be obtained from a plot:

- Coordination number of the absorber atom
- The Debye-Waller factor
- The average inter-atomic distance
- The average deviation in the average inter-atomic distance

The Debye-Waller factor corresponds to the mean square relative displacement of the absorber and back-scatterer atoms, and causes damping of the EXAFS signal. The value of the Debye-Waller factor increases with increasing temperature, because a higher thermal energy leads to more vibrations between atoms.

The number of parameters that can be reliably determined from the data is limited, mainly depending on the quality of the data. A common practice during a fit of EXAFS spectra is to constrain certain parameters, to increase the accuracy of other parameters during the fit. The amplitude factor (S_0^2) between inelastic and elastic scattering is often constraint during a fitting procedure. The assuming it is constant for a given element. The value can for instance be obtained from a fit with a spectrum from a metal foil, which has a low signal to noise ratio, and thereafter used during the fit of a sample.

The mean free path and the amplitude factor can be calculated by FEFF, and the fit was performed with IFEFFIT. Both methods are incorporated in the Demeter software package.[29]

5. Experimental methods

5.1. Synchrotron

The experimental measurements were performed at the European Synchrotron Radiation Facility (ESRF) in Grenoble, France. The facility consists of an electron storage ring with an operating energy of 6 GeV and a circumference of 884 meter. The experiments of this project were conducted at BM23, which is a multipurpose x-ray absorption spectroscopy (XAS) beamline. The beamline is a so-called energy scanning beamline, which makes a scan through the different x-ray energies.

The experiments were performed between the 5th and the 9th of March, the 20th of April and the 11th of May. During the experiments in March all promoted samples were tested on their noble metal edges, and the silver promoted sample together with the unpromoted samples were tested on the cobalt edge. In March and April, the silver and rhenium promoted sample were re-tested at a higher reaction temperature. During the beam time in March the catalysts were tested at 220℃, which is the same temperature that was used during the catalytic tests performed earlier. The experiments in April and May were performed at 260 ℃, because the catalyst shows an optimum in activity at that temperature.

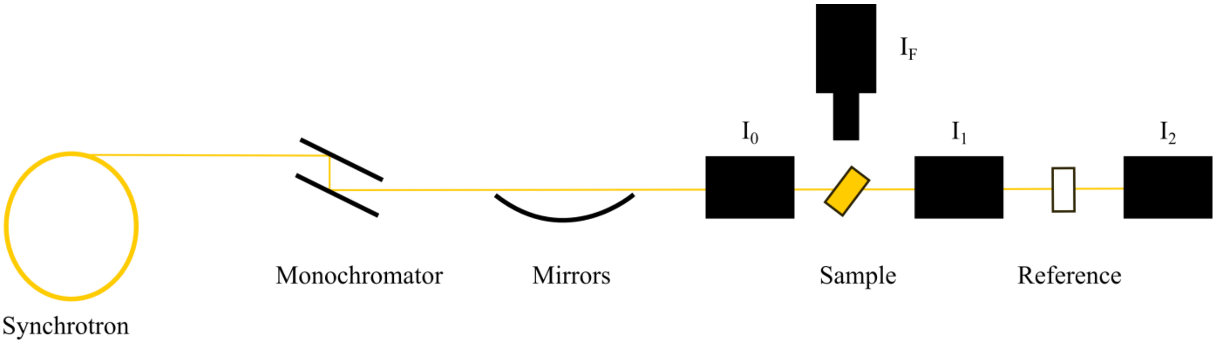

Figure 16: A schematic image of the layout of BM23.

5.2. The multipurpose x-ray absorption spectroscopy beamline BM23

5.2.1. The Optics hutch of BM23

The optics hutch is located behind the bending magnet and contains the monochromator and focusing lenses. The monochromator is used to select one wavelength of the polychromatic x-ray beam coming from the bending magnet. It consists of two mirrors of silicon crystals which have different lattice spacing: 111, 311 and 511. Because different silicon crystals can be used, according to Bragg's law, the monochromator can be used to select x-ray photons of an wide energy range of 4 to74 keV ($3.1\cdot10^{-1}$ to $1.6\cdot10^{-2}$ nm). The second mirror of the monochromator is the same as the first mirror and makes sure the beam is reflected into its original direction towards the experimental hutch.

In table 1 the different energies of the studied absorption edges are displayed.

Table 1: Binding energies (in KeV) for the K and L edges of the elements measured during this project. The energies that are used during experiments are shown in bold. Reproduced from:[30]

	Z	K	L_{III}	L_{II}	L_I
Co	27	**7.71**			
Ru	44	22.11	**2.84**	2.97	3.22
Ag	47	25.51	**3.35**	3.52	3.81
Re	75	71.68	**10.54**	11.96	12.53
Pt	78	78.39	**11.56**	13.27	13.88

5.2.2. The experimental hutch of BM23

The experimental hutch is the place for the sample environment and the detectors to perform measurements. Depending on the experiment, the sample might be in the open air, vacuum, in a capillary or contained within a custom-designed cell. During experiments performed in a capillary the sample can be heated (300-800 K) and reactant gasses can be flowed to the sample to perform in-situ experiments. By using a custom-designed cell, samples can be cooled with liquid nitrogen or helium or heated by an electric oven or laser light. Furthermore, some cells can work at elevated pressures while performing x-ray absorption scans. The used capillary holder or the cell are mounted on a stand which has electric motors that position the sample very precisely with respect to the beam.[27]

The detectors that are available are ionization chambers and fluorescence detectors. The ionization chambers are a part of the fixed beamline set-up and can be filled with He, N_2, Ar and Kr. Usually the ionization chambers are set-up for maximal spectral resolution, with a higher gas pressure in I_1 than in I_0, resulting in an absorption of 30% for I_0 and 70% for I_1. For a fluorescence measurement there are several detectors available, such as a Vortex®-60EX x-ray detector and a Ge 13 element detector.

5.2.3. The control room of BM23

The control room of BM23 is equipped with multiple computers to control the experiment. The computers work with a linux based command-line interface.

5.3 XAFS on Co/TiO_2

The XAFS experiments on the Co/TiO_2 were conducted using quartz capillaries with varying thickness. Thinner capillaries were used for experiments at lower x-ray energies, where the absorption of quartz is more profound. For the measurements on the ruthenium, silver and cobalt edges, capillaries with an inner diameter of 1.5 mm, and a wall thickness of 0.01 mm were used. For the measurements on the platinum and rhenium edges, capillaries with an inner diameter of 1.6 mm and a wall thickness of 0.04 mm were used. Per measurement about 50 mg of sample was place inside the capillary with quartz wool on both sides. The thermocouple was inserted into the capillary, and then the capillary was glued in between the tubes of the gas inlet and gas outlet.

The set-up was placed in the experimental hutch and the gas tubes were connected to the sample holder. For the experiments pure H_2, CO and He gasses were used, which were supplied by gas bottles. A set-up made of Swagelok® tubes and valves combined with Bronkhorst® mass-flow controllers was used to mix the gasses and ensure a constant flow of 10 ml/min. The oven and the thermocouple of the sample holder were connected to a temperature controller. Gas outlet was connected to the mass spectrometer to acquire online results. Thereafter, the sample was aligned to the beam by moving the motors of the workspace in the x, y and z direction.

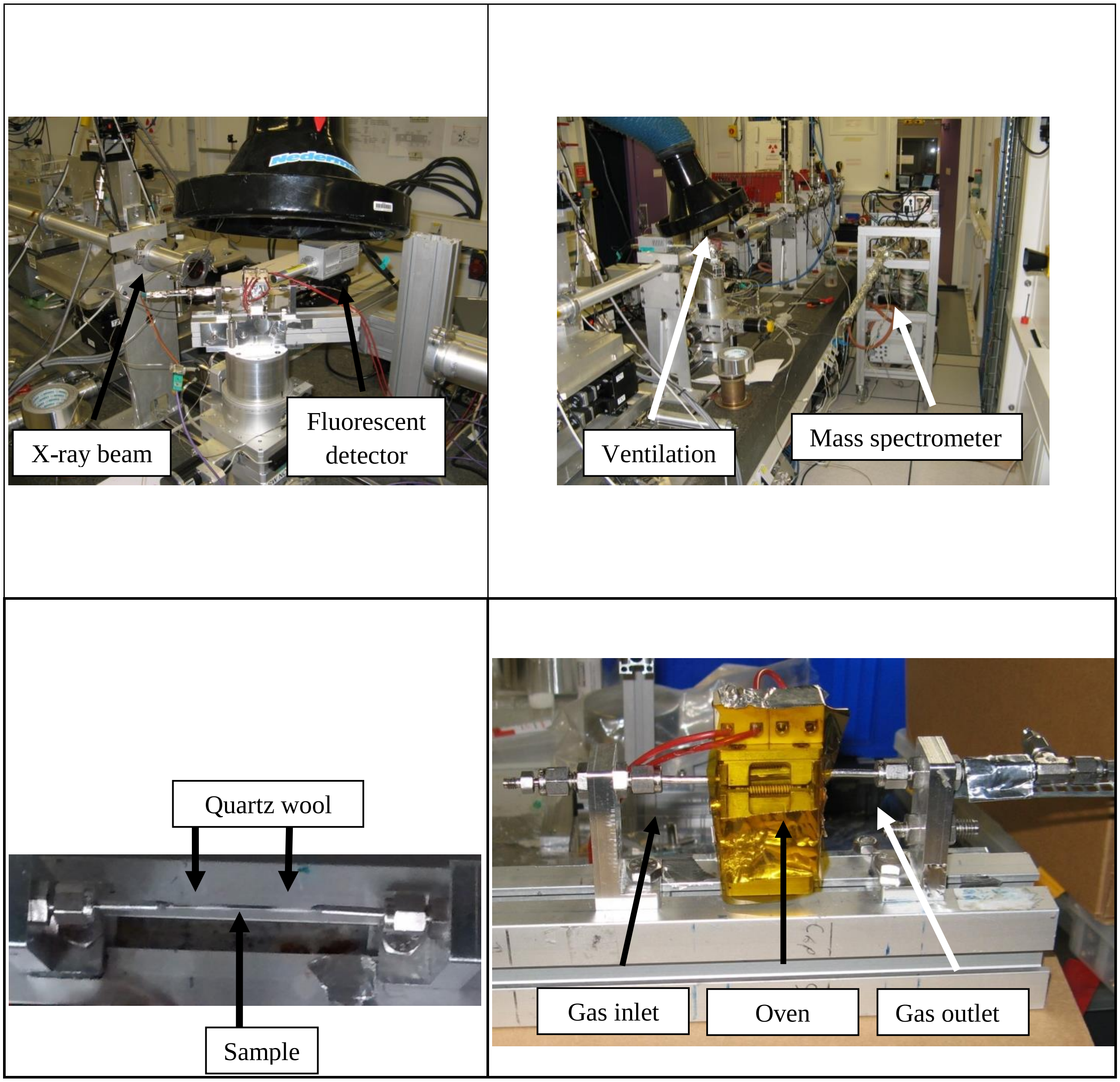

Figure 17: Pictures of the in-situ setup used during experiments. On the picture right below the capillary with the sample can be seen.

5.4 Experimental procedure

Each experiment was performed according to a standard procedure. For the experiments in April and May a measurement/reaction temperature of 260℃ was used, instead of 220℃, to increase the activity of the catalyst. The experiments were performed at a constant gas flow of 10 ml/min.

1. Sample was dried for 10 minutes in Helium at 50 ℃
2. Sample was reduced with a ramp of 5 ℃/min to 350 ℃ (~1 hour), in H_2 (20%)/He.
3. Temperature at 350 ℃ for 30 minutes, in H_2 (20%)/He
4. Temperature is lowered to 220 ℃ with a ramp of 5 ℃/min, in H_2 (20%)/He
5. EXAFS scan of the reduced sample, in H_2 (20%)/He
6. Once the temperature is stabilized switch to H_2/CO (2:1)
7. EXAFS scan of the sample during synthesis

During this project the Demeter software package was used, which consists of Athena, Arthemis and Hephaestus. Athena was used for data extraction while Arthemis was used for fitting of the spectra in R-space.[29]

6. Results

6.1 Catalyst activation

Results on silver, ruthenium, rhenium and platinum promoted Co/TiO_2 with a cobalt/noble metal ratio of 0.0143 at. have been obtained. Before each measurement, the catalyst was activated by reduction of cobalt oxide to metallic cobalt. This change in oxidation state is visible in the XANES area of the cobalt and noble metal edges (figures 18,19). During the reduction procedure, the noble metal will be reduced at lower temperatures than the cobalt. In figure 19 the XANES of rhenium can be seen during the reduction, which lowers above a temperature of 228 ℃. The experiments were performed at an x-ray scanning beamline which is not suitable for analysis on a sample with a temperature ramp, because the recording of each scan takes a few minutes. Therefore, the exact reduction temperature of rhenium oxide could not be distinguished.

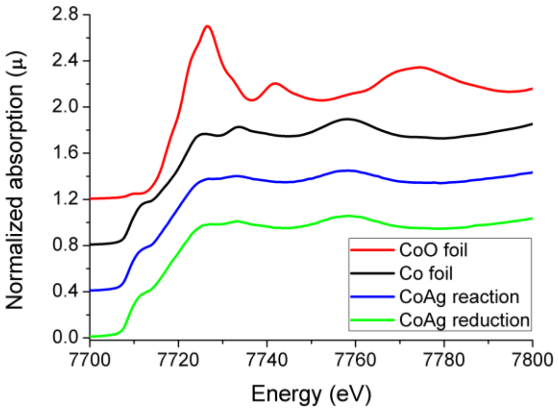

Figure 18: The XANES spectra of silver promoted Co/TiO_2, cobalt foil and a cobalt(II)oxide foil, measured at the cobalt k-edge (7.7 KeV). The spectrum of cobalt(II)oxide foil has a different shape compared to the metallic cobalt and the silver promoted Co/TiO_2, indicating that the cobalt of the catalyst is reduced.

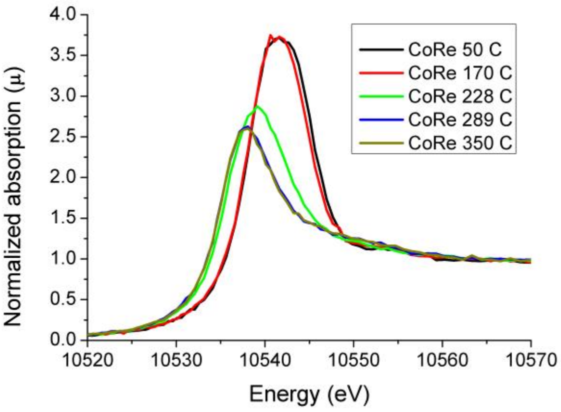

Figure 19: The XANES spectra of the rhenium L_3-edge (10.5 KeV) taken during reduction of rhenium promoted Co/TiO_2 are displayed. From the legend can be seen which scan was taken at which temperature. When the temperature increases, the jump becomes lower indicating the presence of metallic rhenium.

6.2 Study of the type and number of nearest neighbours

6.2.1. Rhenium promoted Co/TiO_2

EXAFS scans were made on the Re L_3-edge of rhenium promoted Co/TiO_2 catalysts after the reduction and during the reaction at 260℃. The resulting spectra in k space and R space can be seen in figure 20 and 21, respectively. The plot in k space has a usable range from 3 to 10 k, for oscillations at higher k values the signal is dominated by noise. By comparing the spectra of the catalyst with the spectrum of a rhenium foil in R space, it is evident that there are no or very little Re-Re interactions in the sample after the reduction and during the reaction. However, the presence of fine structure indicates there are neighboring atoms around rhenium atoms. To obtain more information about the type and number of neighboring atoms some fits were performed with the Re-Re and Co-Re distances using Iffefit.

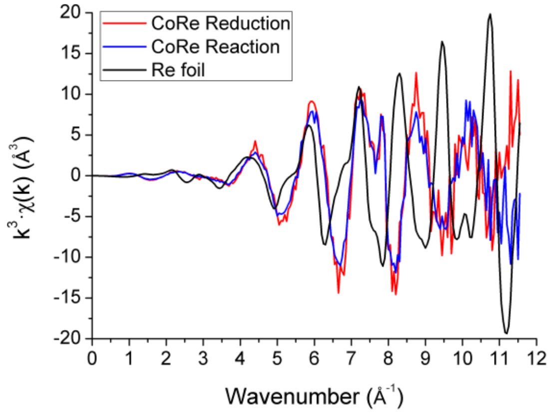

Figure 20: The EXAFS of rhenium promoted Co/TiO_2 and rhenium foil, plotted in k space and a k weight of 3.

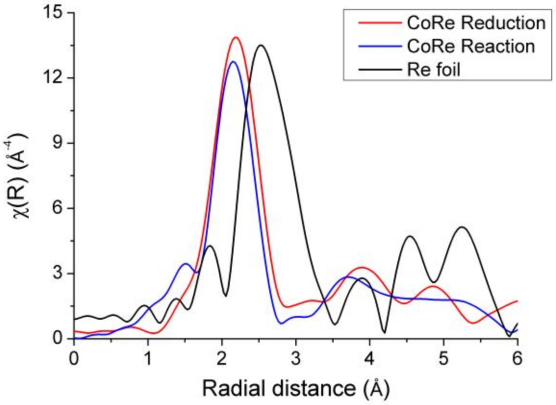

Figure 21: The EXAFS of rhenium promoted Co/TiO_2 and rhenium foil, plotted in R space.

The attempt to fit the spectra with the Re-Re distance did not lead to decent results; however the fit with the Co-Re distance was successful for both the spectra after reduction and during reaction. The fitting was performed in R space with a range of 1.60 - 2.79. The S_0^2 for the fits was obtained from a platinum foil, because a usable rhenium foil was not available. In the figures 22-25 the plot of the spectrum and the fit are shown in k space and R space, and in table 2 the results of the fits are shown.

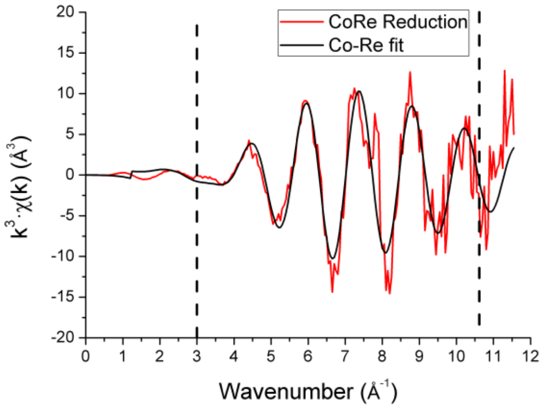

Figure 22: The plot of rhenium promoted Co/TiO$_2$ in k-space after reduction, fitted with the Co-Re distance. The used range was 3.000-10.617.

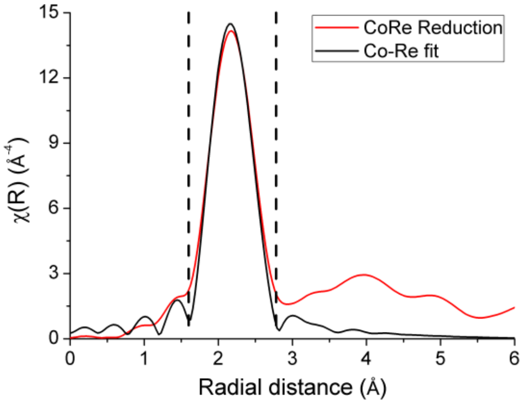

Figure 23: The plot of rhenium promoted Co/TiO$_2$ in R-space after reduction, fitted with the Co-Re distance with a range of 1.60 - 2.79.

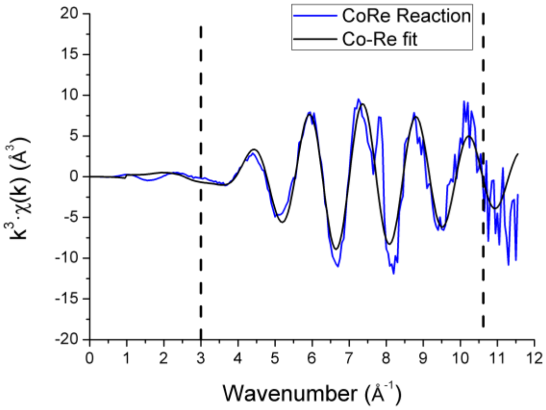

Figure 24: The plot of rhenium promoted Co/TiO$_2$ in k-space during reaction, fitted with the Co-Re distance. The used range was 3.000-10.617.

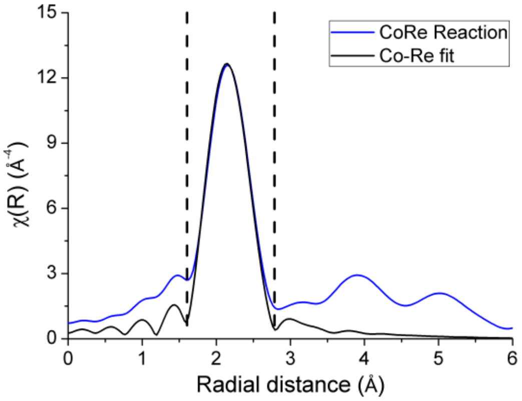

Figure 25: The plot of rhenium promoted Co/TiO$_2$ in R-space during reaction, fitted with the Co-Re distance with a range of 1.60 - 2.79.

Table 2: Results of the fits of the rhenium promoted sample. *The S_0^2 was obtained from a platinum foil; the other results were obtained from a rhenium foil.

Sample		S_0^2	N	R (Å)	σ^2 (Å^2)	E_0 (eV)
Rhenium foil	Re-Re	0.81±0.07*	*12*	2.74±0.03	0.0024±0.0007	11.6±0.8
CoRe Reduction	Co-Re	*0.81*	9±2	2.52±0.05	0.009±0.002	5±3
CoRe Reaction	Co-Re	*0.81*	7±2	2.53±0.06	0.008±0.002	4±3

It appears that the rhenium atoms are on average surrounded by 9 cobalt atoms while during the reaction the rhenium atoms are surrounded by 7 cobalt atoms (table 2). This result indicates that the rhenium particles are incorporated in cobalt particles, forming a bimetallic alloy. The relatively low coordination numbers of 9 and 7 can be explained by the presence of rhenium atoms close to the surface of the cobalt particles. Another explanation can be that the atoms are present in a distorted cobalt crystal structure, because the rhenium atoms are bigger than the cobalt atoms.

6.2.2. Silver promoted Co/TiO_2

EXAFS scans were made on the silver k-edge of silver promoted Co/TiO_2 catalysts after the reduction and during the reaction during two different experiments at different temperatures, at 260℃ and at 220℃. The resulting spectra in k space and R space plotted with the spectra of a silver foil, can be seen in figures 26-29. By comparing the spectra in figure 26, it can be concluded that for the signal at low k-values the oscillations are not in the same phase. For higher k values, starting from 6 $Å^{-1}$, the oscillations of the foil are in approximately the same phase as the oscillations of the sample. When the same spectra are plotted in R space by a Fourier transform (range: 3.000 - 9.942 k), it can be seen that the silver promoted sample shows a high resemblance with the silver foil. This indicates the presence of Ag-Ag bonds in the sample, and moreover there are none or very few Co-Ag bonds. The most probable explanation of this result is the presence of small, isolated silver particles on the support of the catalyst. In figure 28 the spectrum of the catalyst taken at 220℃ is displayed which has a lower resolution than the spectrum has taken at 260℃. However, the resemblance with the silver foil is even stronger; the oscillations are in the same phase over a broader range, from 2 to 12 k. Unfortunately there was an technical error while measuring the sample during the reaction, which caused a lower resolution for the measurement. Despite the varying resolution, it can be clearly seen from figure 27 and 29 that Ag-Ag interactions are present in the sample.

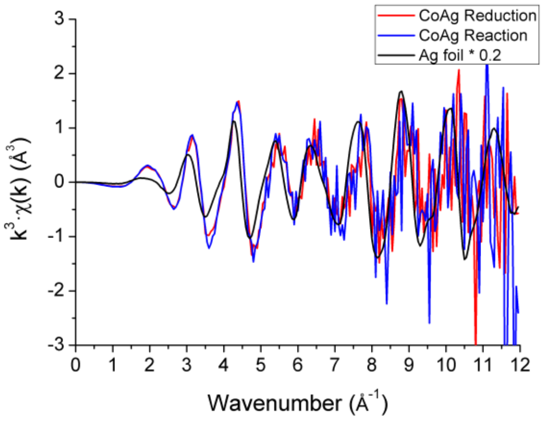

Figure 26: The plot of silver promoted Co/TiO_2 and silver foil at 260 ℃ plotted in k space with a k weight of 3.

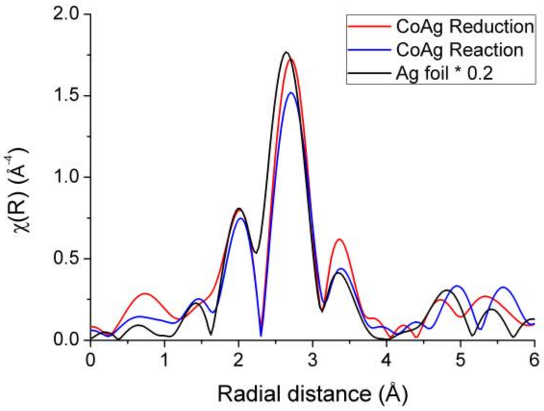

Figure 27: The plot of silver promoted Co/TiO_2 and silver foil at 260 ℃ plotted in R space.

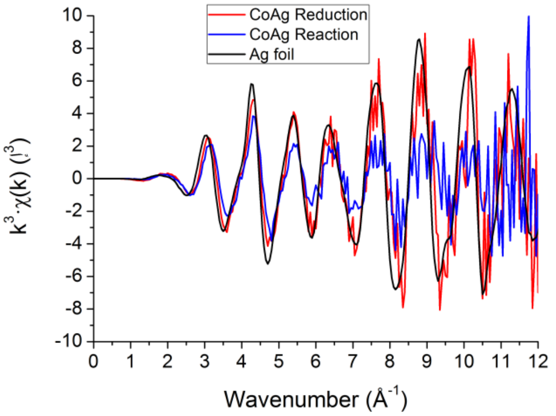

Figure 28 : The plot of silver promoted Co/TiO_2 and silver foil at 220 ℃ plotted in k space with a k weight of 3.

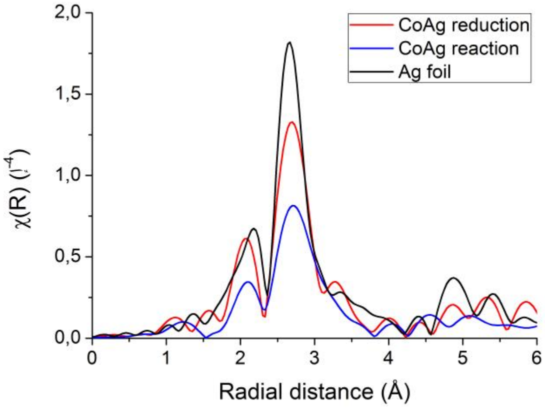

Figure 29 : The plot of silver promoted Co/TiO_2 and silver foil at 220 ℃ plotted in R space.

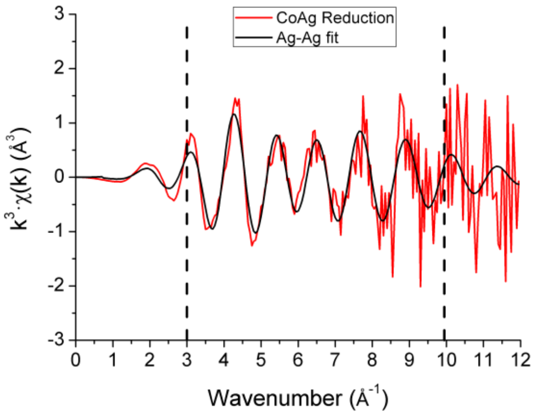

Figure 30: The plot of silver promoted Co/TiO_2 in k-space after reduction at 260℃, fitted with the Ag-Ag distance with a range of 3.00-9.94

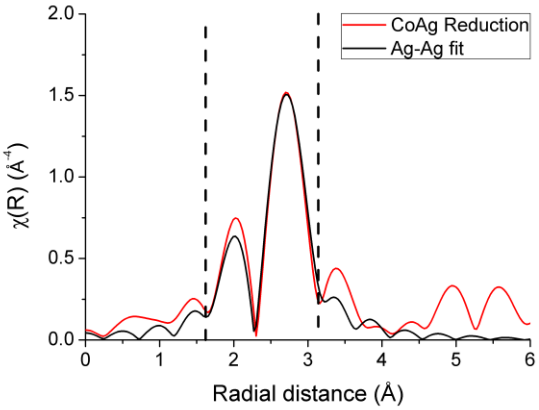

Figure 31: The plot of silver promoted Co/TiO_2 in R-space after reduction at 260℃, fitted with the Ag-Ag distance with a range of 1.70-3.20.

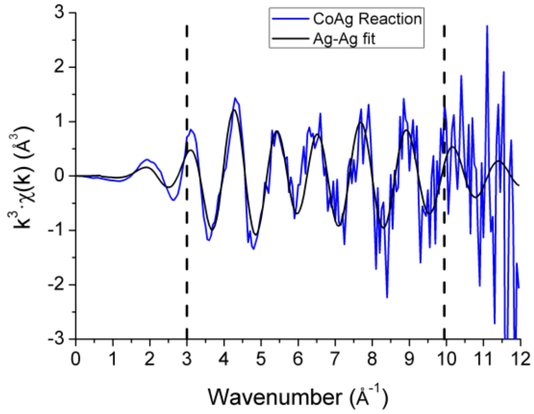

Figure 32: The plot of silver promoted Co/TiO_2 in k-space after reaction at 260℃, fitted with the Ag-Ag distance with a range of 3.00-9.94.

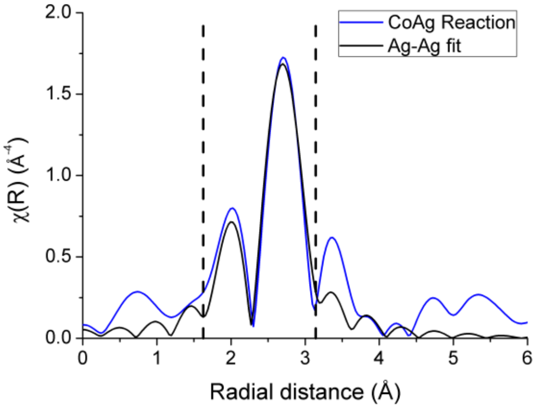

Figure 33: The plot of silver promoted Co/TiO_2 in R-space after reaction at 260℃, fitted with the Ag-Ag distance with a range of 1.70-3.20.

Sample	fit	S_0^2	N	R (Å)	σ^2 (Å^2)	E_0 (eV)
Silver foil	Ag-Ag	0.83±0.04	*12*	2.87±0.03	0.0096±0.0004	1.0±0.4
CoAg Reduction	Ag-Ag	*0.83*	4.1±0.6	2.85±0.05	0.018±0.001	2.1±0.9
CoAg Reaction	Ag-Ag	*0.83*	4.1±0.8	2.83±0.06	0.016±0.002	1.7±1.4

Table 3: Results of the fit of the scan performed at 260℃.

Sample	fit	S_0^2	N	R (Å)	σ^2 (Å^2)	E_0 (eV)
CoAg Reduction	Ag-Ag	*0.83*	10.6±0.8	2.85±0.05	0.0101±0.0006	1.2±0.5
CoAg Reaction	Ag-Ag	*0.83*	10±2	2.84±0.05	0.017±0.002	3±2

Table 4: Results of the fit of the scan performed at 220℃.

In figures 30-33 and table 3 the results of the fits of the scans at 260℃ are shown, while in table 4 the results of the fits of the scans at 220℃ are shown. Both scans are fitted with the Ag-Ag distance, to determine the amount of silver atoms coordinated around the absorber silver atoms. The fit of the scan taken at 260℃ result in a coordination number of 4 silver atoms, which indicates the presence of small silver clusters of approximately 10 atoms.[31]

6.2.3. Ruthenium promoted Co/TiO_2

EXAFS scans were performed on the Ru K-edge of Ruthenium promoted Co/TiO_2 catalysts after the reduction and during the reaction at 220℃. The resulting spectra in k space and R space are shown in figures 34 and 35. The plot in k space has a usable k-range from about 2.5 to 10.5. By comparing the spectra of the catalyst with the spectrum of a ruthenium foil can be concluded that the vibrations for low k values the oscillations are not in the same phase. For higher k values, the oscillations of the foil are in the same phase as the oscillations of the sample. When the same spectra are plotted in R-space by a Fourier transform with a k range of 2.562-10.654, the presence of species at more or less the same length as the Ru-Ru distance in the Ruthenium foil becomes visible. In order to get more information about the type of atoms surrounding the Ruthenium atoms in the sample at fit in Arthemis, using Iffefit, was performed with the Ru-Ru and Co-Ru distance (figures 36-39).

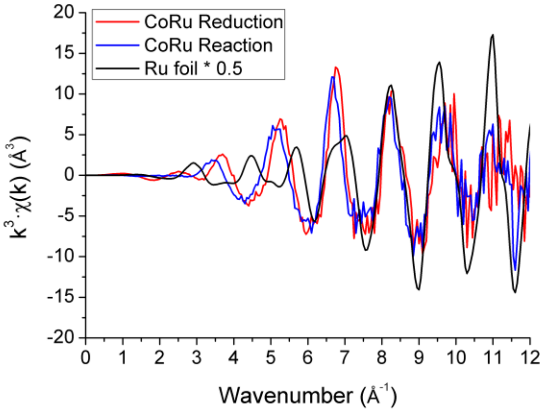

Figure 34: The plot of ruthenium promoted Co/TiO_2 and ruthenium foil at 220℃ plotted in k space with a k weight of 3.

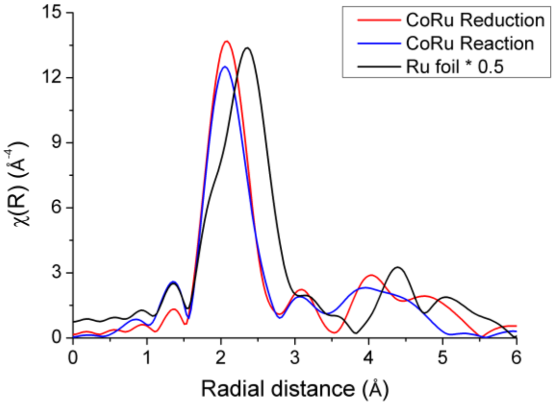

Figure 35: The plot of ruthenium promoted Co/TiO_2 and ruthenium foil at 220℃ plotted in R space.

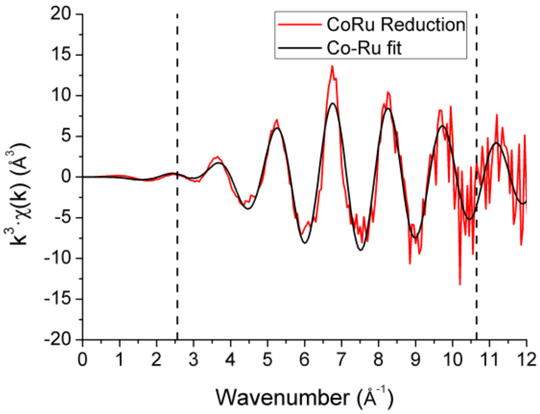

Figure 36: The plot of ruthenium promoted Co/TiO$_2$ in k space after reduction, fitted with the Co-Ru distance, with a range of 2.56-10.65.

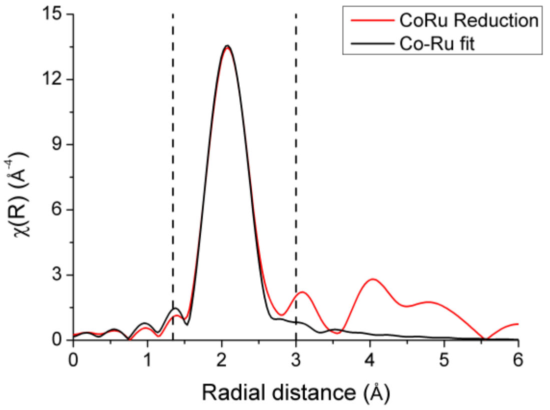

Figure 37: The plot of ruthenium promoted Co/TiO$_2$ in R space after reduction, fitted with the Co-Ru distance, with a range of 1.34-3.00.

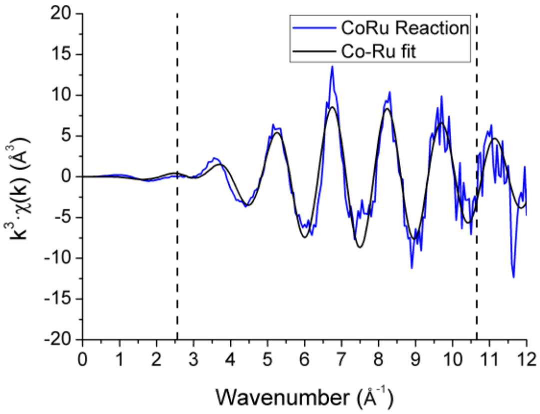

Figure 38: The plot of ruthenium promoted Co/TiO$_2$ in k space after reduction, fitted with the Co-Ru distance, with a range of 2.56-10.65.

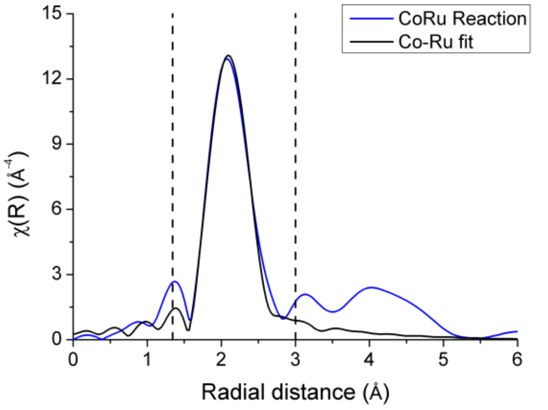

Figure 39: The plot of ruthenium promoted Co/TiO$_2$ in k space after reduction, fitted with the Co-Ru distance, with a range of 1.34-3.00.

The fit in Arthemis (figures 36-39) indicates that there were Co-Ru interactions in the sample. In table 5 the results can be seen of the sample during reduction and during reaction.

Table 5: Results of the fit of the Ruthenium promoted Co/TiO$_2$.

Sample	fit	S_0^2	N	R (Å)	σ^2 (Å^2)	E_0 (eV)
Ruthenium foil	Ru-Ru	0.8±0.1	*12*	2.67±0.03	0.003±0.001	4±1
CoRu Reduction	Co-Ru	*0.792*	7.4±0.7	2.5±0.1	0.0075±0.0007	1±1
CoRu Reaction	Co-Ru	*0.792*	6.4±0.9	2.5±0.1	0.006±0.001	0±2

6.2.4. Platinum promoted Co/TiO$_2$

EXAFS scans were performed on the Pt L$_3$-edge of platinum promoted Co/TiO$_2$ catalysts after the reduction and during the reaction at 220℃. The resulting spectra in k space and R space can be seen in figure 40 and 41. The plot in k space has a usable k range from about 2.5 to 10.5. By comparing the spectra of the catalyst with the spectrum of a platinum foil can be concluded that the vibrations for low k values the oscillations are in the same phase. For higher k values, the oscillations of the foil are not in the same phase as the oscillations of the sample. When the same spectra are plotted in R space by a Fourier transform with a k range of 2.562-10.654, it can be seen that are neighboring atoms at more or less the same length as the Pt-Pt distance in the platinum foil. In order to get more information about the type of atoms surrounding the platinum atoms in the sample, the spectra were fitted in Arthemis (figures 42-45, table 6).

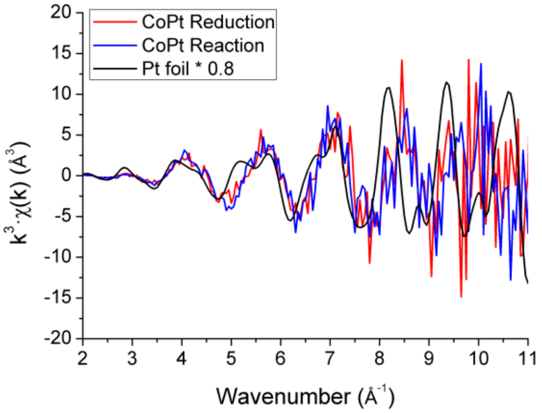

Figure 40: The plot of platinum promoted Co/TiO$_2$ and platinum foil at 220 ℃ plotted in k space with a k weight of 3.

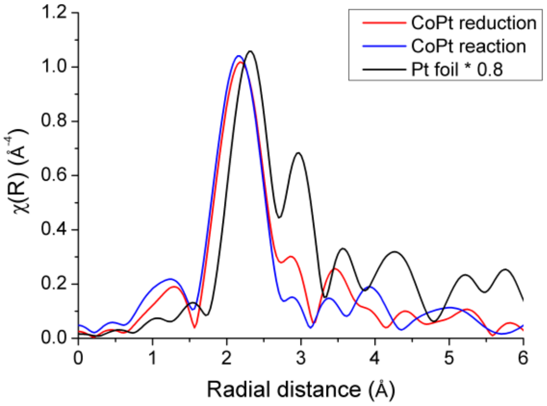

Figure 41: The plot of platinum promoted Co/TiO$_2$ and platinum foil at 220 ℃ plotted in k space with a k weight of 3.

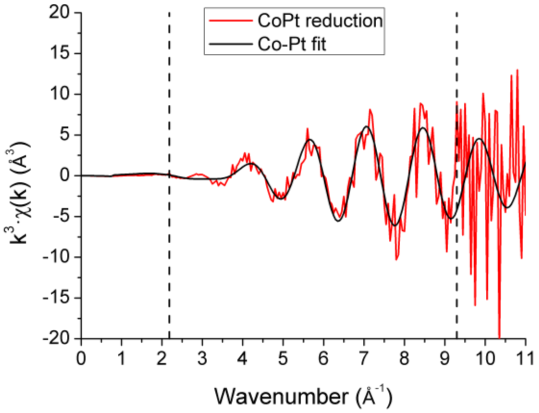

Figure 42: The plot of platinum promoted Co/TiO_2 in k space after reduction, fitted with the Co-Pt distance, with a range of 2.56-10.65.

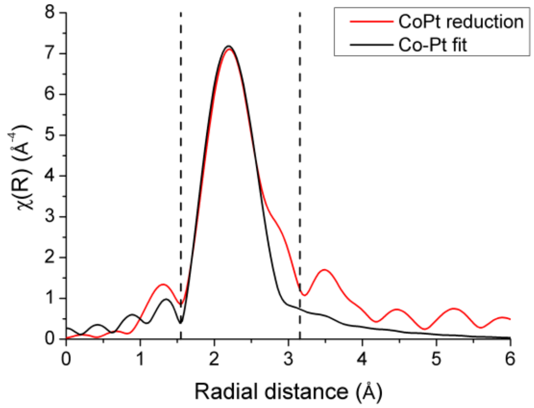

Figure 43: The plot of platinum promoted Co/TiO_2 in R space after reduction, fitted with the Co-Pt distance, with a range of 1.55-3.15.

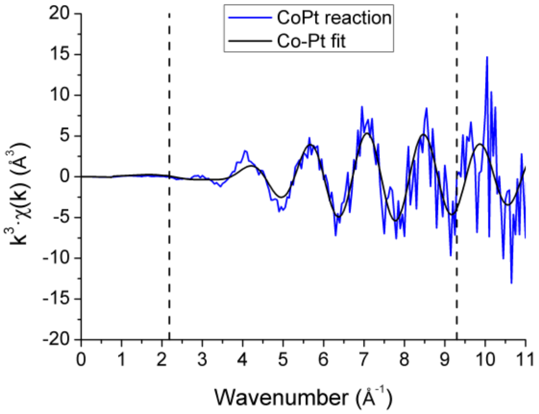

Figure 44: The plot of platinum promoted Co/TiO_2 in k space after reduction, fitted with the Co-Pt distance, with a range of 2.56 - 10.65.

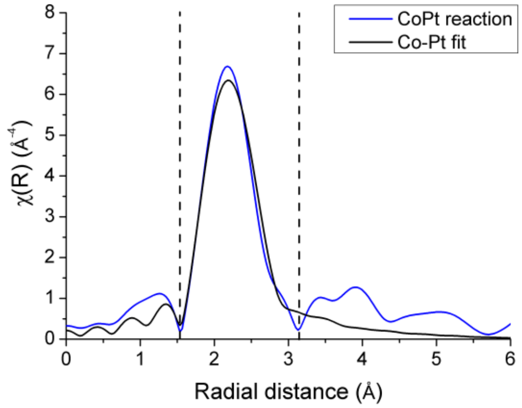

Figure 45: The plot of platinum promoted Co/TiO_2 in R space after reduction, fitted with the Co-Pt distance, with a range of 1.55-3.15.

Table 6: Results of the fit of the platinum promoted Co/TiO_2.

Sample	fit	S_0^2	N	R (Å)	σ^2 (Å^2)	E_0 (eV)
Platinum foil	Pt-Pt	0.81±0.07	*12*	2.75±0.05	0.0035±0.0005	7.4±0.5
CoPt Reduction	Co-Pt	*0.81*	6±1	2.6±0.2	0.007±0.002	2±2
CoPt Reaction	Co-Pt	*0.81*	6±1	2.6±0.2		

The fitting of the platinum spectra appeared to be quite difficult because there are two types of interactions: the Co-Pt and Pt-Pt. The fitting with the Co-Pt distance gave the best results, and therefore these results were used for further analysis (table 6). In order to get better results from the fit, the Debye-Waller factor and the E_0 were assumed to be constant for the sample after the reduction and during the reaction. Since these factors are mainly dependent on the temperature, this is a reasonable assumption. The fit resulted in a coordination number of 6 cobalt atoms each platinum atom, both after reduction and during reaction.

7. Discussion

Promotion of cobalt catalyst with noble metals may lead to bimetallic alloy formation of cobalt and the noble metal or formation of cobalt and noble metal phases. The bimetallic particles are predominantly formed during oxidative treatments after catalyst synthesis.[12] Further mixing of cobalt and the noble metal can occur during reduction of the catalyst. Unfortunately, given the limited resolution of the spectra off the catalyst obtained during this project did not have resolution to detect the second shell in the absorption spectra. Therefore, only oxygen atoms were detected as neighboring atoms in the oxidized state of the catalyst for the cobalt and noble metal. For the analysis the data, only the results of the first shell of the catalyst in active state are used.

For the rhenium promoted Co/TiO_2, Co-Re interactions were observed, with a coordination number of 9 after the reduction and 7 during the reaction. Furthermore, there appeared to be no Re-Re interactions in the sample. For the rhenium promoted catalyst a Co-Re coordination of 9 was observed after the reduction of the catalyst, while a coordination number of 7 was observed during the reaction. This could indicate a structural change of the catalyst during synthesis when it is exposed to the reactants. An explanation for the decreased cobalt coordination number could be that rhenium atoms are more exposed at surface of cobalt particles which might be caused by the local migration of atoms. However, it is hard to draw good conclusions because both measurements have an uncertainty of 2 which means that the apparent structural change is in the margin of error. It would be desirable to further investigate this measurement by performing EXAFS measurements with a higher resolution. Co-Re interactions on rhenium promoted cobalt catalyst were also observed by Davis and Holmen using alumina as support.[16,17] In both studies, no direct Re-Re bonding contribution was observed, leading to the conclusion that Re remains present on the surface as isolated from other Re atoms, in intimate contact with the cobalt metal cluster. It can be concluded that in rhenium promoted cobalt catalyst bimetallic particles are formed independent of the support.

For the silver promoted catalyst, Ag-Ag interactions were found to be present in the sample which indicates the presence of a silver phase. The silver atoms have a coordination number of 4 which indicates that statistically the silver phase should consist of approximately 10 atoms.[31] This result on silver promoted catalysts is deviating from the results of the other catalysts, where cobalt-noble metal alloys were formed. The formation of small silver clusters on silver promoted catalysts was also obtained by a study of Davis et al. on alumina.[32] Interestingly, despite the difference in structure of the catalyst the catalyst shows an increased apparent turnover frequency, similar to the catalyst promoted with the other noble metals (figure 4a). However, the cobalt time yield of the catalyst is lower for the silver promoted catalyst than for the ruthenium, platinum and rhenium promoted catalyst. The three fold increase in turn over frequency is only observed if the cobalt particle dispersion for spend catalyst is used. The apparent turnover frequency if the cobalt particle dispersion of fresh catalyst is used is about 1,5 fold the apparent turnover frequency of the unpromoted catalyst.[1] Possible explanations for the less distinct increase in cobalt time yield could be that silver is less good in splitting hydrogen during the reduction procedure and therefore has a lower degree of reduction, or that silver does not catalyze the hydrogenation of coke on the surface of the catalyst.

The ruthenium promoted cobalt catalysts were found to have Ru-Co interactions with a coordination number of approximately 6 or 7. This indicates that the ruthenium is most likely present at or near the surface of the cobalt particles. Similar results were obtained by Iglesia et al. on ruthenium promoted

Co/TiO_2. They reported a Ru-Co coordination number of 5 to 6. However, also Ru-Ru interactions were found with a coordination number of 6 to 8, indicating the presence of a ruthenium phase. After calcination of the catalyst, increased mixing between the cobalt and the ruthenium was observed, with increased mixing for calcination at higher temperatures. During this project no Ru-Ru interactions were observed, which can be explained by the different synthesis procedure. Iglesia et al. used a sequential impregnation method whereas during this project a co-impregnation was used. By using a solution of two precursors a better mixing of the two metals is ensured.[33]

The platinum promoted cobalt catalysts were found to have Pt-Co interactions with a coordination number of 6. Furthermore, the results also indicate that some Pt-Pt interactions could be present. During previous studies on platinum promoted cobalt catalysts on alumina and silica, only Pt-Co interactions were found.[18,19] An explanation for this relatively low coordination number of 6 for the Pt-Co interactions obtained during this project could be that the platinum atoms are coordinated to other platinum atoms and form small clusters of a few atoms. Therefore the platinum promoter could have different behavior on titania than on silica or alumina. However, the resolution of the measurements is not sufficient to draw good conclusions.

8. Conclusions

During this project successful EXAFS measurements were performed on noble metal promoted Co/TiO_2 Fischer-Tropsch catalysts. The catalysts were tested in-situ after reduction and during Fischer-Tropsch synthesis. The measurements were performed by detecting the x-ray fluorescence when measuring the platinum and rhenium L_{III} edge and the ruthenium and silver K edge.

During EXAFS measurements on rhenium promoted and ruthenium promoted Co/$TiO_{2,}$ cobalt-noble metal interactions were formed. Considering the coordination numbers of both promoter metals, the noble metal atoms are most probably present at the surface of the cobalt particles. During the EXAFS measurements on silver promoted catalyst, Ag-Ag coordination with a coordination number of 4 was observed. This indicates there are small silver particles cluster present of ~10 atoms on the surface of the catalyst. On the platinum promoted Co/$TiO_{2,}$ mainly Pt-Co interactions were observed with a low coordination number were observed. However, some Pt-Pt interactions could also be present but unfortunately the resolution of the measurement is not good enough to draw definite conclusions.

Suggestions for further measurements could be to perform in-situ EXAFS experiments under pressure, to study the effect of elevated pressures on noble metals during Fischer-Tropsch synthesis. It is known that when performing catalytic experiments under pressure, the composition of the catalyst changes, which could affect the mixing of the noble metal and the cobalt. Another interesting experiment could be to perform IR spectroscopy experiments with CO as a probe to study the absorption on the active sites. These experiments could give more lucidity about the ability of noble metals to hydrogenate coke deposits on the surface of cobalt particles and thereby increasing the availability of cobalt active sites, such as described by Iglesia et al.[34]

9. Acknowledgements

For this project I would like to acknowledge a number of people. Firstly, my daily supervisor at the ESRF: Dr. Giovanni Agostini, who organized the experiments on the beamline and explained everything I needed to know to perform the measurements. Furthermore, I would like to thank my other supervisors: Dr. Sakura Pascarelli, Dr. Andrei Pethoukov and Prof. Dr. Frank de Groot for help and support to make it possible to perform this very interesting and instructive internship at the ESRF.

10. References

1. Oenema, J. Noble metal promotion on Co/TiO2 Fischer-Tropsch catalysts. (2015).

2. Eschemann, T. O., Oenema, J. & de Jong, K. P. Noble metal promotion for Co/TiO2 Fischer-Tropsch catalysts. *Catal. Today* (2015).

3. Van Vliet, O. P. R., Faaij, A. P. C. & Turkenburg, W. C. Fischer–Tropsch diesel production in a well-to-wheel perspective: A carbon, energy flow and cost analysis. *Energy Convers. Manag.* **50,** 855–876 (2009).

4. Van de Loosdrecht, J. *et al. Comprehensive Inorganic Chemistry: Fischer-Tropsch Synthesis: Catalysts and Chemistry*. *Comprehensive Inorganic Chemistry II* **7,** (Oxford: Elsevier, 2013).

5. Khodakov, A. Y., Chu, W. & Fongarland, P. Advances in the development of novel cobalt Fischer-Tropsch catalysts for synthesis of long-chain hydrocarbons and clean fuels. *Chem. Rev.* **107,** 1692–744 (2007).

6. Shell website. (2015).

7. Heriot-Watt University. *BP Statistical Review of World Energy*. (2014).

8. Dry, M. E. Fischer–Tropsch reactions and the environment. *Appl. Catal. A Gen.* **189,** 185–190 (1999).

9. Liu, G., Larson, E. D., Williams, R. H., Kreutz, T. G. & Guo, X. Making Fischer−Tropsch Fuels and Electricity from Coal and Biomass: Performance and Cost Analysis. *Energy & Fuels* **25,** 415–437 (2011).

10. Chorkendorff, I. & Niemantsverdriet, J. W. (Hans). *Concepts of Modern Catalysis and Kinetics*. (Wiley-VCH Verlag GmbH & Co. kGaA, 2007).

11. Morales, B. Y. F. & Weckhuysen, B. M. Promotion Effects in Co-based Fischer – Tropsch Catalysis. **19,** (2006).

12. Iglesia, E., Soled, S. L., Fiato, R. A. & Via, G. H. Bimetallic synergy in co-ru catalysts. *J. Catal.* **143,** 345–368 (1993).

13. Ma, W., Jacobs, G., Keogh, R. a., Bukur, D. B. & Davis, B. H. Fischer–Tropsch synthesis: Effect of Pd, Pt, Re, and Ru noble metal promoters on the activity and selectivity of a 25%Co/Al2O3 catalyst. *Appl. Catal. A Gen.* **437-438,** 1–9 (2012).

14. Diehl, F. & Khodakov, A. Y. Promotion of Cobalt Fischer-Tropsch Catalysts with Noble Metals : a Review. **64,** 11–24 (2009).

15. Storsæter, S., Borg, Ø., Blekkan, E. A. & Holmen, A. Study of the effect of water on Fischer-Tropsch synthesis over supported cobalt catalysts. *J. Catal.* **231,** 405–419 (2005).

16. Rønning, M., Nicholson, D. G. & Holmen, A. In situ EXAFS study of the bimetallic interaction in a rhenium-promoted alumina-supported cobalt Fischer-Tropsch catalyst. *Catal. Letters* **72,** 141–146 (2001).

17. Jacobs, G., Chaney, J. a., Patterson, P. M., Das, T. K. & Davis, B. H. Fischer-Tropsch synthesis: Study of the promotion of Re on the reduction property of Co/Al2O3 catalysts by in situ EXAFS/XANES of Co K and Re LIII edges and XPS. *Appl. Catal. A Gen.* **264,** 203–212 (2004).

18. Jacobs, G. *et al.* Fischer-Tropsch synthesis: study of the promotion of Pt on the reduction property of Co/Al2O3 catalysts by in situ EXAFS of Co K and Pt L3 in situ edges and XPS. *J. Synchrotron Radiat.* **11,** 414–422 (2004).

19. Dees, M. The influence of sulfur and carbonaceous deposits on the selectivity and activity of Pt/Co catalysts in hydrocarbon reactions. *J. Catal.* **119,** 376–387 (1989).

20. Jacobs, G. *et al.* Group 11 (Cu, Ag, Au) promotion of 15%Co/Al2O3 Fischer–Tropsch synthesis catalysts. *Appl. Catal. A Gen.* **361,** 137–151 (2009).

21. Newville, M. *Fundamentals of XAFS*. *Consortium for Advanced Radiation Sources* (2004). doi:10.2138/rmg.2014.78.2

22. Fornasini, P. Synchrotron Radiation: Fundamentals, Methodologies and Applications. in (eds. Mobilio, S., Vlaic, G. & Margherita di Pula, S.) 129–171 (2001).

23. Koningsberger, D. C., Mojet, B. L., Dorssen, G. E. Van & Ramaker, D. E. XAFS spectroscopy ; fundamental principles and data analysis. **10,** 143–155 (2000).

24. Groot, F. M. F. De. Site-selective XAFS : a new tool for catalysis research. **10,** 179–186 (2000).

25. Fornasini, P. *Welcome to XAFS : a friendly but not so short tutorial*. (2014).

26. Pascarelli, S. Fundamentals of X-ray Absorption Fine Structure: basic principles. 1–67 (2015).

27. Various authors. ESRF website. *http://www.esrf.eu/* (2015).

28. Pascarelli, S. Hercules presentation, Part II Fundamentals of X-ray Absorption Fine Structure : data analysis. (2015).

29. Ravel, B. & Newville, M. ATHENA, ARTEMIS, HEPHAESTUS: data analysis for X-ray absorption spectroscopy using IFEFFIT. 537–541 (2005). doi:10.1107/S0909049505012719

30. Brennan, S. & Cowan, P. A suite of programs for calculating x-ray absorption, reflection and diffraction performance for a variety of materials at arbitrary wavelengths. *Rev. Sci. Instrum. 63* 850 (1992).

31. Agostini, G. *et al.* Effect of different face centered cubic nanoparticle distributions on particle size and surface area determination: A theoretical study. *J. Phys. Chem. C* **118,** 4085–4094 (2014).

32. Jermwongratanachai, T. *et al.* Fischer–Tropsch synthesis: Comparisons between Pt and Ag promoted Co/Al2O3 catalysts for reducibility, local atomic structure, catalytic activity, and oxidation–reduction (OR) cycles. *Appl. Catal. A Gen.* **464-465,** 165–180 (2013).

33. Eschemann, T. O., Bitter, J. H. & de Jong, K. P. Effects of loading and synthesis method of titania-supported cobalt catalysts for Fischer–Tropsch synthesis. *Catal. Today* (2013). doi:10.1016/j.cattod.2013.10.041

34. Iglesia, E., Soled, S., Fiato, R. & Via, G. Bimetallic synergy in cobalt ruthenium Fischer-Tropsch synthesis catalysts. *J. Catal.* (1993).